AIAA 2008-2873

Validation of a hybrid CAA method. Application to the case of a ducted diaphragm at low Mach number

Mélanie Piellard*
Delphi Thermal Systems
L-4940 Bascharage, Luxembourg

Christophe Bailly†
Laboratoire de Mécanique des Fluides et d'Acoustique
École Centrale de Lyon & UMR CNRS 5509, 69134 Ecully, France
& Institut Universitaire de France

In this work, a hybrid method of aerodynamic noise computation is first validated, and then applied to investigate the noise radiated by a low Mach number flow through a diaphragm in a duct. The simulation method is based on a two steps approach relying on Lighthill's acoustic analogy, assuming the decoupling of noise generation and propagation. The first step consists of an incompressible Large Eddy Simulation of the turbulent flow field, during which the Lighthill's source term is recorded. In the second step, a variational formulation of Lighthill's Acoustic Analogy using a finite element discretization is solved in the Fourier space. A general validation is performed with the case of two corotating vortices to assess the proper definition of the source term; the exit of turbulent structures from the computational domain is accounted for by a spatial filtering. This method is applied to a realistic three-dimensional diaphragm at low Mach number flow; the aerodynamic flow features are detailed, showing good agreement with both experimental and numerical studies in similar conditions. The acoustic computation is currently in progress.

I. Introduction

In the automotive industry, the design of thermal comfort products involves working on the acoustic performance. The development of a simulation method able to accurately predict the aeroacoustic noise has been launched in order to better understand noise generation mechanisms in complex geometries involving internal low Mach number flows. In the present industrial context, the simulation time has to be reasonable, and the method implementation has to involve commercial or free computing codes. Among the available hybrid methods, Curle's extension[1] of Lighthill's analogy[2] is the most appropriate to this specific problem: the surface effects are accounted for, while the volume source definition imposes accuracy only locally, avoiding costly compressible CFD computations. Indeed, when applying Ffowcs-Williams and Hawkings[3] method for instance, all information relevant for the definition of acoustic sources has to be propagated to the integration surface. The acoustic simulation tool has also to easily tackle complex geometries; this is achieved when working with finite elements methods. The Computational Fluid Dynamics software choice is only driven by the tool availability in the company; any CFD software can be used, provided that proper Large Eddy Simulation is implemented; the same holds regarding the acoustic propagation tool. In the present work, all the computations are performed with Actran/LA[4] and Fluent.[5]

The paper is organized as follows. Theoretical foundations are recalled in §II. The considered method is established with academic studies in §III, in order to address some issues intrinsically linked to a hybrid

*PhD student, melanie.piellard@delphi.com.
†Professor, AIAA Senior Member, christophe.bailly@ec-lyon.fr.

approach, such as source term definition, spatial truncation of noise sources leaving the computational domain and interpolation of sources from the CFD mesh to the acoustic mesh. Then, the method is applied in §IV to investigate the noise radiated by a low Mach number flow through a ducted diaphragm. A similar configuration has been previously studied by Gloerfelt *et al*[6] using direct noise computation, which constitutes a reference solution for the present work; links are also made to similar configurations extensively examined previously, such as plane sudden expansions (PSE) and backward facing steps (BFS).

II. Theory

The prediction method is a two step hybrid approach relying on Lighthill's acoustic analogy,[2] assuming the decoupling of noise generation and propagation. The first step consists of an incompressible Large Eddy Simulation of the turbulent flow field, during which a source term is transiently recorded. In the second step, a variational formulation of Lighthill's Acoustic Analogy discretized by a finite element discretization is solved in the Fourier space, leading to the radiated noise up to the free field thanks to the use of infinite elements.[4]

II.A. Variational formulation of Lighthill's Acoustic Analogy

The implementation of Lighthill's Acoustic Analogy was firstly derived by Oberai *et al*,[7] refer also to Actran User's Guide[4] and Sandbodge *et al*[8] for instance. The starting point is Lighthill's equation:

$$\frac{\partial^2}{\partial t^2}(\rho-\rho_0) - c_0^2\frac{\partial^2}{\partial x_i \partial x_i}(\rho-\rho_0) = \frac{\partial^2 T_{ij}}{\partial x_i \partial x_j} \tag{1}$$

with

$$T_{ij} = \rho u_i u_j + \delta_{ij}\big((p-p_0) - c_0^2(\rho-\rho_0)\big) - \tau_{ij} \tag{2}$$

where ρ is the density and ρ_0 its reference value in a medium at rest, c_0 is the reference sound velocity, T_{ij} is Lighthill's tensor, u_i, u_j are the components of the fluid velocity, p is the pressure and τ_{ij} is the viscous stress tensor. The strong variational statement associated to equation (1) is written as:

$$\int\limits_{\Omega} \left(\frac{\partial^2}{\partial t^2}(\rho-\rho_0) - c_0^2\frac{\partial^2}{\partial x_i \partial x_i}(\rho-\rho_0) - \frac{\partial^2 T_{ij}}{\partial x_i \partial x_j}\right)\delta\rho \, d\mathbf{x} = 0 \quad \forall\, \delta\rho \tag{3}$$

where $\delta\rho$ is a test function and Ω designates the computational domain. Following Green's theorem, the previous equation is integrated by parts along spatial derivatives:

$$\int\limits_{\Omega} \left(\frac{\partial^2}{\partial t^2}(\rho-\rho_0)\,\delta\rho + c_0^2\frac{\partial}{\partial x_i}(\rho-\rho_0)\frac{\partial \delta\rho}{\partial x_i} + \frac{\partial T_{ij}}{\partial x_j}\frac{\partial \delta\rho}{\partial x_i}\right) d\mathbf{x} = \int\limits_{\partial\Omega=\Gamma} \left(c_0^2\frac{\partial}{\partial x_i}(\rho-\rho_0)n_i + \frac{\partial T_{ij}}{\partial x_j}n_i\right)\delta\rho \, d\Gamma(\mathbf{x})$$

with n_i the normal pointing outwards of Ω. Replacement of T_{ij} with equation (2) leads to

$$\int\limits_{\Omega} \left(\frac{\partial^2}{\partial t^2}(\rho-\rho_0)\,\delta\rho + c_0^2\frac{\partial}{\partial x_i}(\rho-\rho_0)\frac{\partial \delta\rho}{\partial x_i} + \frac{\partial T_{ij}}{\partial x_j}\frac{\partial \delta\rho}{\partial x_i}\right) d\mathbf{x} = \int\limits_{\Gamma} \frac{\partial}{\partial x_j}\left(\rho u_i u_j + (p-p_0)\delta_{ij} - \tau_{ij}\right) n_i \,\delta\rho \, d\Gamma(\mathbf{x})$$

After having defined Σ_{ij} as

$$\Sigma_{ij} = \rho u_i u_j + (p-p_0)\delta_{ij} - \tau_{ij}\,, \tag{4}$$

the equation on the acoustic density fluctuations $\rho_a = \rho - \rho_0$ is finally derived:

$$\int\limits_{\Omega} \left(\frac{\partial^2 \rho_a}{\partial t^2}\,\delta\rho + c_0^2\frac{\partial \rho_a}{\partial x_i}\frac{\partial \delta\rho}{\partial x_i}\right) d\mathbf{x} = -\int\limits_{\Omega} \frac{\partial T_{ij}}{\partial x_j}\frac{\partial \delta\rho}{\partial x_i}\, d\mathbf{x} + \int\limits_{\Gamma} \frac{\partial \Sigma_{ij}}{\partial x_j} n_i\,\delta\rho\, d\Gamma(\mathbf{x}) \tag{5}$$

In this formulation, called the variational formulation of Lighthill's analogy, two source terms are present: a volume term and a surface term. Recalling the momentum equation

$$\frac{\partial \rho u_i}{\partial t} + \frac{\partial \rho u_i u_j}{\partial x_j} = -\frac{\partial}{\partial x_j}(p\delta_{ij} - \tau_{ij}) \tag{6}$$

the surface source term is rewritten as

$$n_i \frac{\partial \Sigma_{ij}}{\partial x_j} = n_i \frac{\partial}{\partial x_j}\big(\rho u_i u_j + (p - p_0)\delta_{ij} - \tau_{ij}\big) = -n_i \frac{\partial}{\partial t}(\rho u_i) \tag{7}$$

Then, if the surface Γ is fixed or vibrating in its own plane, expression (7) reduces to zero. In the following of this study, only fixed surfaces are considered and the surface source term vanishes. Moreover, the following notation is adopted for the volume source term:

$$S_i = \frac{\partial T_{ij}}{\partial x_j}. \tag{8}$$

II.B. Spectral formulation

The problem is solved in the frequency domain. Equation (5) is thus written in the spectral space thanks to a Fourier transform. The time Fourier transform is defined as

$$\mathcal{F}[\phi(\mathbf{x},t)] = \phi(\mathbf{x},\omega) = \int_{-\infty}^{\infty} \phi(\mathbf{x},t) e^{-i\omega t} dt \tag{9}$$

where $\omega = 2\pi f$ is the angular pulsation. With the following notations for harmonic perturbations of any quantity ϕ

$$\phi(\mathbf{x},t) = \widetilde{\phi}(\mathbf{x}) e^{i\omega t}$$

the spectral equation solved within Actran is written as:

$$\int\limits_{\Omega} \left(-\omega^2 \widetilde{\rho}_a \, \delta\rho + c_0^2 \frac{\partial \widetilde{\rho}_a}{\partial x_i} \frac{\partial \delta\rho}{\partial x_i} \right) d\mathbf{x} = -\int\limits_{\Omega} \frac{\partial \widetilde{T}_{ij}}{\partial x_j} \frac{\partial \delta\rho}{\partial x_i} \, d\mathbf{x} + \int\limits_{\Gamma} \frac{\partial \widetilde{\Sigma}_{ij}}{\partial x_j} \, n_i \, \delta\rho \, d\Gamma(\mathbf{x}) \tag{10}$$

II.C. Associated analytical resolution

A two-dimensional spectral solution of Lighthill's equation has also been developed for validation. Green's functions are used to solve Lighthill's equation, which allows to express the solution of an inhomogeneous wave equation as an integral. The free space Green function $G(\mathbf{x},t|\mathbf{x},\tau)$ is the response, at position $\mathbf{x}$ and time t, to an impulse signal from $\mathbf{y}$ emitted at time τ. It is defined as the physical solution of the inhomogeneous wave equation

$$\frac{\partial^2 G(\mathbf{x},t|\mathbf{x},\tau)}{\partial x_i^2} - \frac{1}{c_0^2} \frac{\partial^2 G(\mathbf{x},t|\mathbf{x},\tau)}{\partial t^2} = \delta(\mathbf{x}-\mathbf{y})\,\delta(t-\tau) \tag{11}$$

where δ is the Dirac generalized function. In the spectral domain, using the convention defined in equation (9), wave equation (11) becomes the Helmholtz equation

$$(\nabla^2 + k^2)\, G(\mathbf{x}|\mathbf{y},\omega) = \delta(\mathbf{x}-\mathbf{y}) \tag{12}$$

where $k = \omega/c_0$ is the wavenumber, and the two-dimensional solution of equation (12) writes

$$G(\mathbf{x}|\mathbf{y},\omega) = \frac{i}{4} H_0^{(2)}(kr) \tag{13}$$

where $H_0^{(2)}$ is the Hankel function of second kind and order 0, and $r = |\mathbf{x}-\mathbf{y}|$. Lighthill's equation (1) can be written on acoustic pressure fluctuations $p_a = p - p_0$ instead of density fluctuations $\rho_a = \rho - \rho_0$, yielding:

$$\nabla^2 p_a - \frac{1}{c_0^2} \frac{\partial^2 p_a}{\partial t^2} = -\frac{\partial^2 T_{ij}}{\partial x_i \partial x_j} \tag{14}$$

In the spectral domain, the inhomogeneous wave equation (14) is transformed into an inhomogeneous Helmholtz equation:

$$(\nabla^2 + k^2)\, p_a(\mathbf{x},\omega) = -\frac{\partial^2 T_{ij}(\mathbf{x},\omega)}{\partial x_i \partial x_j} \tag{15}$$

The solutions of Lighthill's equation expressed as integral formulations are obtained by convoluting the Green's function with the source term of equation (14):

$$p_a = c_0^2 \rho_a = -G \star \frac{\partial^2 T_{ij}}{\partial x_i \partial x_j}$$

Using the two-dimensional expression (13) leads to the following solution:

$$p_a(\mathbf{x}, \omega) = -\frac{i}{4} \iint\limits_{S_0(\mathbf{y})} H_0^{(2)}(kr) \frac{\partial^2 T_{ij}(\mathbf{x}, \omega)}{\partial y_i \partial y_j} \, \mathrm{d}\mathbf{y} = -\frac{i}{4} \iint\limits_{S_0(\mathbf{y})} \frac{\partial^2 H_0^{(2)}(kr)}{\partial y_i \partial y_j} T_{ij}(\mathbf{x}, \omega) \, d\mathbf{y}$$

in free space. Analytical developments using the properties of Hankel functions lead to the two-dimensional spectral solution of Lighthill's equation:

$$p_a(\mathbf{x}, \omega) = -\frac{i}{4} \iint\limits_{S_0(\mathbf{y})} \left[k^2 \frac{r_i r_j}{r^2} H_0^{(2)}(kr) - k \left(\frac{2 r_i r_j}{r^3} - \frac{\delta_{ij}}{r} \right) H_1^{(2)}(kr) \right] T_{ij}(\mathbf{x}, \omega) \, \mathrm{d}\mathbf{y} \tag{16}$$

Equation (16) will be used in the following to assess results obtained with the variational formulation of Lighthill's analogy.

II.D. Practical application of the method

The method consists of coupling a CFD code with a finite element acoustic software where the variational formulation of Lighthill's Acoustic Analogy is implemented. Here follow the different steps of a practical computation, provided that a transient solution of the flow field has already been obtained:

1. an analysis of the flow field allows to determine in which region(s) of the flow acoustic source terms will be considered; an acoustic mesh is built on the whole region of interest for acoustics, with fine elements in the region(s) of source terms and bigger elements elsewhere;

2. a mesh file containing the coordinates of the nodes where source terms are to be considered is created;

3. this mesh file is read by the CFD code, presently Fluent v6.3.26,[5] and the acoustic nodes are localized in the CFD domain;

4. a database containing the time history of the source term vector $\mathbf{S} = [S_1 \quad S_2 \quad S_3]^t$ in three dimensions at each node of the acoustic mesh is created;

5. a utility program reads the data and transforms the source terms from time to spectral domain; these spectral data, written as the vector $\widetilde{\mathbf{S}} = [\mathfrak{Re}(\widetilde{S_1}) \quad \mathfrak{Im}(\widetilde{S_1}) \quad \mathfrak{Re}(\widetilde{S_2}) \quad \mathfrak{Im}(\widetilde{S_2}) \quad \mathfrak{Re}(\widetilde{S_3}) \quad \mathfrak{Im}(\widetilde{S_3})]^t$, are stored in a specific exchange format;

6. the acoustic computation is performed with Actran/LA,[4] with reading of the spectral source terms.

III. Application of the hybrid method to some academic cases

In this section, three issues, associated to the use of previously described hybrid method, are addressed. The source term definition, the spatial truncation of noise sources leaving the computational domain, and the interpolation of sources from the CFD mesh to the acoustic mesh are successively discussed.

III.A. Source term definition

The definition of the source term has to be clearly assessed for this particular implementation of Lighthill's Acoustic Analogy; indeed, Lighthill's tensor can be computed based on the total velocity $\mathbf{u}$ (superscript t), or based on the fluctuating velocity $\mathbf{u}' = \mathbf{u} - \mathbf{u}_0$, where $\mathbf{u}_0$ is the mean velocity field (superscript f), leading to the two following source terms

$$T_{ij}^t = \rho u_i u_j \qquad \text{and} \qquad T_{ij}^f = \rho u_i' u_j' \tag{17}$$

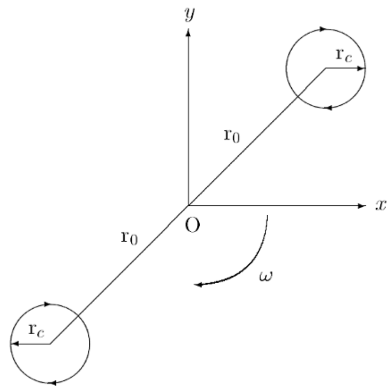

(a)

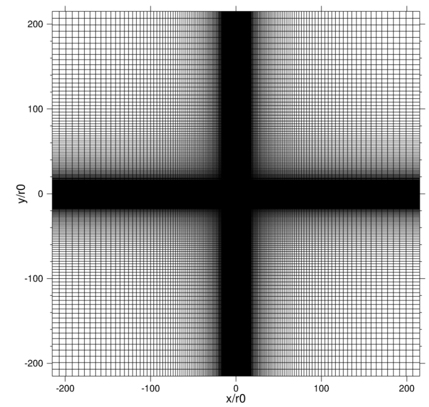

(b)

Figure 1. Two corotating vortices in a medium at rest. (a): Scheme of the vortices system from Bogey.[10] (b): CFD mesh used in this work.

As Bogey *et al*[9] pointed out, among others, the appropriate source term definition is specific to the implementation of the hybrid method. These authors have shown that fluctuating velocities have to be used when working with the Linearized Euler Equations, while total velocities give better results using an analytical solution of Lighthill's Acoustic Analogy. In the first case, the convection effects are accounted for in the propagation operator while in the latter, no convection is considered in the propagation operator; therefore convection effects have to be described in the source term.

In order to investigate this point, the evolution of two corotating vortices is studied; vortices are firstly placed in a medium at rest, and then in a shear layer. This study presents the advantage of discarding other issues cited previously. Indeed, the system of vortices involves no convection out of the computational domain, clearing the spatial truncation issue; moreover, no interpolation is made between CFD and acoustic meshes. The objective here is to understand the physics underlying in the hybrid method of noise computation; therefore, Direct Numerical Simulation and Direct Noise Computation will be used, by means of Fluent, to minimize numerical errors, while incompressible Large Eddy Simulation is the targeted CFD modeling for real applications.

III.A.1. Two corotating vortices in a medium at rest

Vorticity acceleration produces an acoustic radiation, as investigated by Powell.[11] This mechanism is highlighted in the particular two-dimensional case of two corotating vortices; the vortices turn around each other before merging, and then form a solely eddy structure. The scheme on Figure 1(a) presents the vortices system:[10] two identical corotating vortices, clockwise rotating are considered; they are separated by the distance $2r_0$. The pair formed by both vortices also rotates clockwise. Each vortex is initialized by its tangential velocity V_θ, using Scully's vortex model in order to avoid any velocity discontinuity at the vortex center:

$$V_\theta(r) = -\frac{\Gamma r}{2\pi(r_c^2 + r^2)}$$

where r is the current distance from the vortex center, Γ the vortex circulation; r_c is the distance at which the vortices tangential velocity is maximal, $V_{max} = \Gamma/4\pi r_c$.

The radii ratio r_c/r_0 is fixed to 0.22, and the rotation Mach number $M = V_{max}/c_0$ is 0.5. According to Powell,[11] in such a configuration, the rotation velocity on the circle of radius r_0 is given by $\omega = \Gamma/4\pi r_0^2$; thus the rotation period is $T = 8\pi^2 r_0^2/\Gamma$ and the rotation Mach number is $M_r = \Gamma/4\pi r_0 c_0$.

A compressible direct numerical simulation, namely without modeling, is performed using the density-based solver of Fluent[a]. Time discretization is explicit with a 4-step Runge-Kutta algorithm, and for spatial discretization a second-order upwind scheme is considered. Results are processed as follows: the acoustic

[a]In the density-based solver of Fluent, density is obtained from the continuity equation while pressure is computed from the equation of state. Continuity, momentum and energy equations are solved simultaneously.

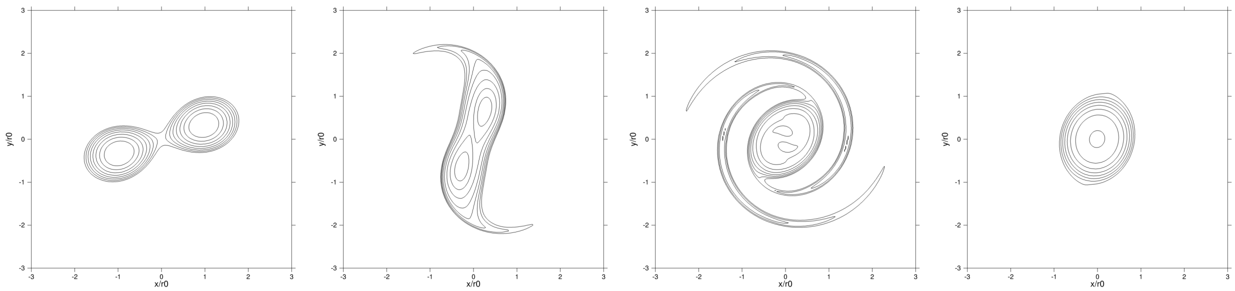

(a) (b) (c) (d)

Figure 2. Two corotating vortices in a medium at rest. Vorticity field obtained after (a): 50000, (b): 106000, (c): 108500 and (d): 120000 time steps. Vorticity isocontours from 10^4 to 1.22×10^5 s^{-1}.

pressure directly computed by CFD in the far field is considered as the reference result; the variational formulation of Lighthill is then carried out, with propagation of the source terms as computed by CFD; finally, the application of Lighthill's equation's analytical solution, as defined in §II.C, serves as an ultimate verification.

Direct Noise Computation

The computational domain extends from $-215\,r_0$ to $215\,r_0$ in each direction and is meshed with 489×489 points, identically in both x and y directions. The mesh size is constant on the first 100 points from the center, with $\Delta = r_0/36 = 1 \times 10^{-4}$ m, and a stretching rate of 4% is applied on the 144 following points. Non Reflecting Boundary Conditions are applied on lateral sides of the computational in order to let the pressure waves leave the domain without disturbances; symmetry boundary conditions are applied on top and bottom boundaries.

At $t = 0$, both vortices are introduced at $(r_0, 0)$ and $(-r_0, 0)$ in a medium at rest (uniform density ρ_0 and pressure p_0). The time step computed by the solver as $\mathrm{CFL} = (c_0 + u_{\max})\Delta t/\Delta$ is fixed at 0.5, leading to a theoretical rotation period of approximately $5260\,\Delta t$. The acoustic source associated to the corotating vortices is a rotating quadrupole. The frequency f_a of the acoustic radiation is twice the rotation frequency of the vortices, due to the symmetry of the structure; the corresponding theoretical acoustic wavelength is $\lambda_a = 29.6\,r_0$.

Merging mechanism

The vortices undergo the following evolution:[12] the vortices first perform several rotations before merging, leading to a single vortex structure. In the present case, the vortices perform 19 rotations keeping well separated from each other, the first rotation at the frequency described by Powell[11] ($T \sim 5360\Delta t$), the following at an ever decreasing frequency with a mean period of $T_{\text{mean}} \sim 5440\Delta t$. Then, during the 20th rotation, the vortices come closer to each other while accelerating the rotation, and quickly merge. Some vorticity filaments are ejected at the fringe of the central eddy structure while both cores are merging, and eventually these filaments are integrated to the remaining big eddy structure. The latter is slightly elliptic, but recovers slowly a circular shape. This merging mechanism is shown on Figure 2, where the vorticity field is represented at different times of the structure evolution.

Acoustic radiation

The pressure signal is recorded at the point $(50\,r_0, 50\,r_0)$ in order to analyze the radiating frequency; its evolution is reported on Figure 3. A transient signal is recognized at the very beginning, with an amplitude higher than the physical signal's one. This transient pressure wave is created by initial conditions, and completely leaves the domain after 7000 time steps without creating spurious waves.

After the transient, three phases with different acoustic radiation are recognized on the pressure signal. Firstly, between time steps 7000 and 108500, the 19 periods of rotation at the mean period $T_{\text{mean}} = 5440\Delta t$ produce an acoustic radiation at the frequency $f_a \sim 2/T_{\text{mean}}$. Then, frequency and levels increase as the

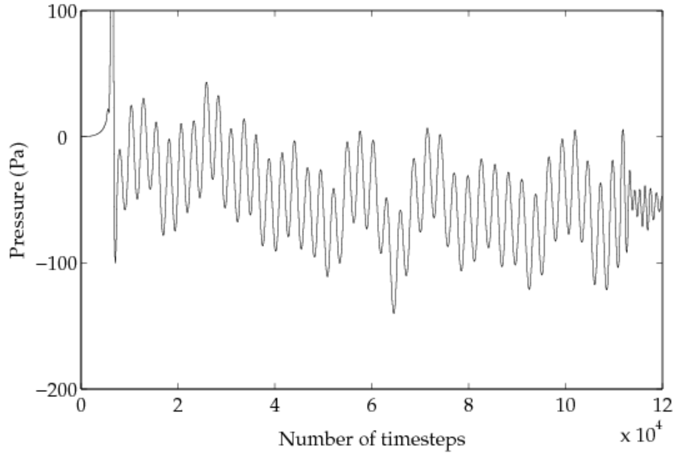

Figure 3. Two corotating vortices in a medium at rest. Static pressure evolution at point $(50\,r_0, 50\,r_0)$ as a function of the number of time steps. Levels in Pa.

vortices come closer to each other. Follows a period with an ever increased frequency, and levels equal to one fourth of levels observed during rotation; this corresponds to the detachment and reattachment of vorticity filaments. Finally, the acoustic radiation decreases while the single vortex structure becomes slowly circular.

Note that the mean of the pressure signal is not equal to the initial pressure p_0; the disturbances are probably due to defaults in the boundary conditions. This low-frequency depression can alter the representation of acoustic pressure waves; in this case, visualizing the dilatation field Θ is more appropriate. In the acoustic far field, dilatation is moreover proportional to the pressure time derivative:

$$\Theta = \nabla \cdot \mathbf{u} = -\frac{1}{\rho_0 c_0^2}\frac{\partial p}{\partial t}$$

The dilatation in far field during the rotation phase is shown in Figure 4. It presents a double spiral structure, corresponding to a rotating quadrupolar acoustic source. The wavelength associated with the acoustic radiation is $\lambda_a = 30\,r_0$, corresponding to a frequency $f_a = 3150\,\mathrm{Hz}$. Figure 5(a) reports how the quadrupole lobes are shifted by 45 degrees with respect to the principal axes of the two vortices, as illustrated in Figure 2(a). Figure 5(b) presents the dilatation in near field, showing the more complex structure composed of two face-to-face quadrupoles.

Application of the hybrid method

The source terms $S_i^t = \partial T_{ij}^t / \partial x_j$ and $S_i^f = \partial T_{ij}^f / \partial x_j$, refer to equations (8) and (17) are recorded during the vortices rotations, between the time steps 10^4 and 10^5, every 20 time steps. They are recorded on the central 200×200 cells where the Cartesian mesh is uniform, corresponding to a square extending from $-2.8\,r_0$ to $2.8\,r_0$ in both directions. A snapshot of these source terms is given in Figure 6.

The source terms are transformed to the spectral space thanks to a Fast Fourier Transform in order to be propagated. The time signal is centered, removing of the mean, and a Hanning filtering is applied before transformation. The acoustic propagation is realized by using these spectral source terms through the implementation (10) described in §II.A.

The mesh used for the acoustic propagation is circular and extends from $-104\,r_0$ to $104\,r_0$ in both directions. It is designed so that its nodes exactly match the CFD cell centers in the region where sources are recorded in order to avoid interpolation[b]; in the remainder of the domain, the mesh size is constrained to $\Delta_{ac} = 5\,\mathrm{mm}$, assuring accurate acoustic propagation up to 11300 Hz. The generally admitted criterion states that one acoustic wavelength has to be discretized by at least 6 elements. The acoustic mesh is displayed in Figure 7(a). The acoustic radiation is then computed in the whole acoustic domain.

[b]In a finite volume code, the velocity is computed at the cell centers; computing and exporting source terms at this location allows a more accurate gradient computation and avoids errors of interpolation from the cell center to the nodes.

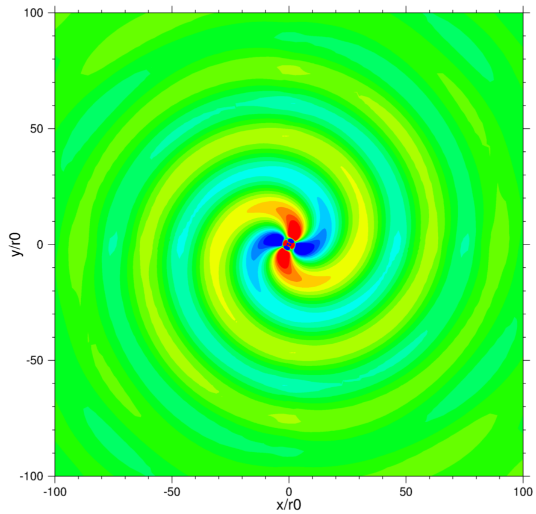

Figure 4. Two corotating vortices in a medium at rest. Dilatation field obtained after 50000 time steps. Color levels from -15 to 15 s^{-1}.

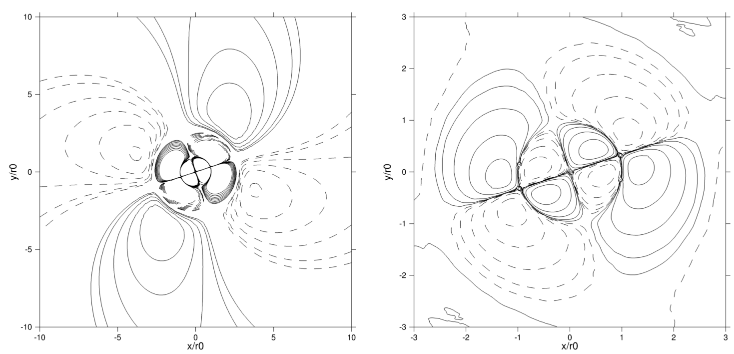

(a) (b)

Figure 5. Two corotating vortices in a medium at rest. Dilatation field obtained after 50000 time steps. (a): 8 isocontours from 8 to 56 s^{-1}. (b): 5 isocontours from 10 to 810 s^{-1}. —— : positive isocontours, − − − : negative isocontours.

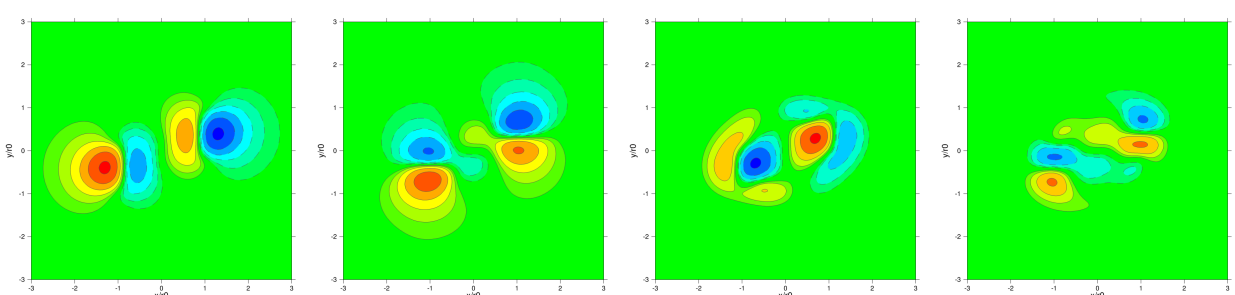

(a) (b) (c) (d)

Figure 6. Two corotating vortices in a medium at rest. Instantaneous source terms obtained after 50000 time steps. (a): S_1^t, (b): S_2^t, (c): S_1^f and (d): S_2^f. 6 isocontours from 6×10^5 to 1.1×10^7 Pa/m.

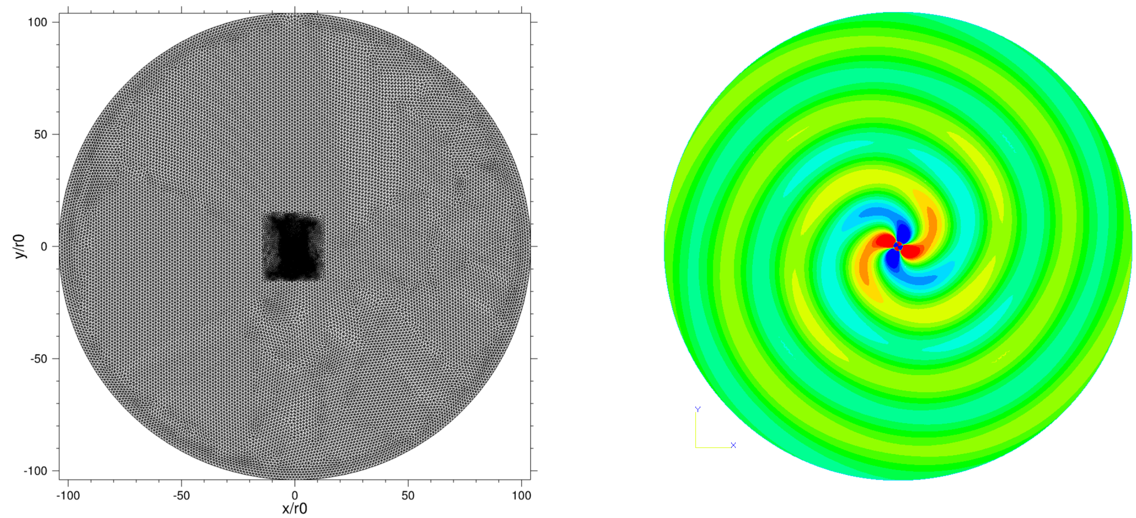

(a) (b)

Figure 7. Two corotating vortices in a medium at rest. (a): Acoustic mesh. (b): Acoustic pressure field (real part) at the main radiation frequency f_a; color levels from -50 to 50 Pa. The domain extends spatially from $-104\,r_0$ to $104\,r_0$ in both directions.

Analytical solution

Similarly, in order to compute the analytical solution of Lighthill's equation, the source terms T^t_{ij} and T^f_{ij} are recorded on the same 200×200 points in the center of the CFD mesh and at the same time steps. After the same treatment on the time signal (mean removing and Hanning filtering), the acoustic pressure radiated by these source terms at point $(50\,r_0, 50\,r_0)$ is computed with equation (16).

Acoustic results

As a first validation, Figure 7(b) presents the acoustic radiation as computed by the variational formulation at the main frequency of radiation $f_a = 3153\,\text{Hz}$. The radiation structure is identical to the one determined by direct computation, namely a rotating quadrupole characterized by its double spiral shape. The levels correspond to the mean amplitude of the pressure signal presented in Figure 3.

Acoustic results are shown in Figure 8 in terms of sound pressure levels radiated at point $(50\,r_0, 50\,r_0)$. The three methods described above are compared: the direct computation, the variational formulation and the analytical resolution of Lighthill's Acoustic Analogy. Moreover, the two possible definitions of the source terms are used in both hybrid resolutions. It is found that the DNS, the variational and analytical resolutions produce the same levels provided the total source terms S^t_i and T^t_{ij} are used.

The agreement is excellent at the radiation frequency $f_a = 3150\,\text{Hz}$. In the low-frequency range, the DNS spectrum departs significantly from spectra obtained using hybrid resolutions; a possible explanation lies in the fact that the direct pressure field is slightly disturbed at low frequencies, as already observed on the time pressure signal in Figure 3; however, these disturbances do not alter the signal at the main radiation frequency. An important feature of the graph is the good correlation between the spectra obtained by both the variational and analytical solutions of Lighthill's Acoustic Analogy; this allows in particular to validate the variational implementation of Lighthill's Acoustic Analogy: in absence of surfaces, both formulations are equivalent. The only disparity between both spectra is found at higher frequencies, above 6000 Hz, where the variational formulation produces higher levels; this is likely to be due to the spatial derivation in the former source term definition, where a factor proportional to M^2 appears.

When using the fluctuating source terms S^f_i and T^f_{ij}, the spectra produced by both hybrid resolutions provide the same results, with levels shifted 10 dB below the DNS spectrum. In the considered case, there is no explicit mean flow, namely in the propagation region, and the source term S^t_i built on the total velocities has to be used.

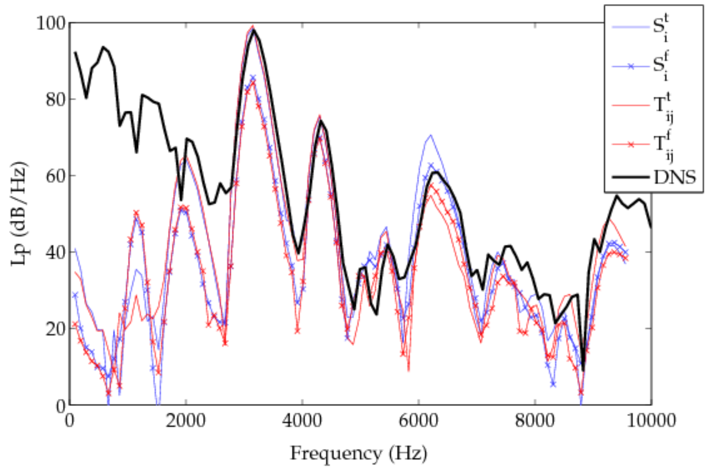

Figure 8. Two corotating vortices in a medium at rest. Sound pressure level radiated at point $(50\,r_0, 50\,r_0)$ obtained with three different methods. Black: direct calculation; blue: variational formulation; red: analytical resolution of Lighthill's Acoustic Analogy. Without symbols: levels obtained using the total source terms S_i^t and T_{ij}^t. With symbols: levels obtained using the fluctuating source terms S_i^f and T_{ij}^f. Levels in dB.

III.A.2. Two corotating vortices placed in a shear layer

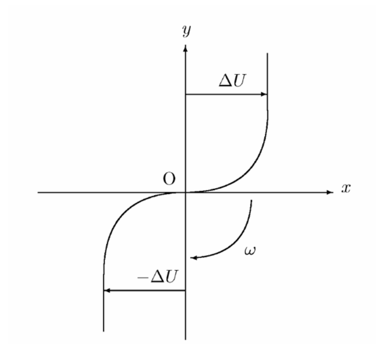

Figure 9. Scheme of the shear layer where vortices are placed.

The addition of a shear layer, previously introduced by Bogey *et al*,[13] allows to study the effects of a mean velocity field on the acoustic radiation. The shear layer is built between two parallel plane flows of opposite velocity ΔU and $-\Delta U$, producing thus a zero mean convection velocity. With this definition, the vortices are not convected by the mean flow field and remain in the center of the computational domain. The shear profile, also shown in Figure 9, is defined with the following hyperbolic-tangent expression of the longitudinal mean velocity:

$$u_0(y) = \Delta U \tanh\left(\frac{u}{2r_0}\right)$$

where r_0, half distance between vortices, is also the shear layer momentum width. The mean velocity is fixed at $\Delta U = c_0/8$.

The same computations as in the previous case are performed: a DNS constitutes the reference results, while the variational and analytical formulations of Lighthill's Acoustic Analogy are successively applied using the complete source terms S_i^t and T_{ij}^t, and using the fluctuating source terms S_i^f and T_{ij}^f in which the mean velocity considered is only the mean shear layer. The mean local velocity due to the constant vortices rotation is no longer considered.

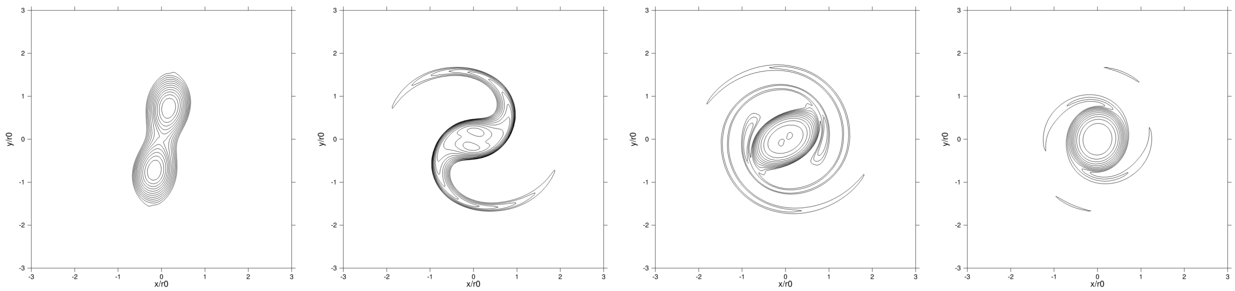

(a) (b) (c) (d)

Figure 10. Two corotating vortices placed in a shear layer. Vorticity field obtained after (a): 20000, (b): 24000, (c): 26000 and (d): 28000 time steps. Vorticity isocontours from 1.5×10^4 to 2.2×10^5 s^{-1}.

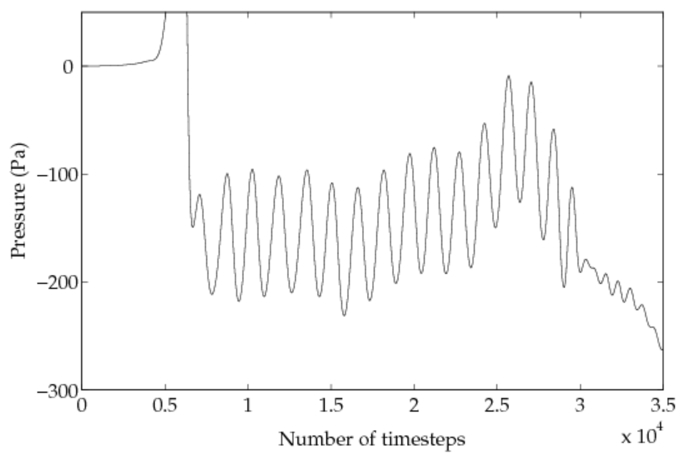

Figure 11. Two corotating vortices placed in a shear layer. Static pressure evolution at point $(50\, r_0, 50\, r_0)$ as a function of the number of time steps. Levels in Pa.

Direct Noise Computation

The computational features are similar to those used before: two identical vortices are introduced at $(r_0, 0)$ and $(-r_0, 0)$ together with the mean shear layer velocity field. The boundary conditions are adapted to allow flow entrance without disturbances: at the upper half of left border and lower half of right border, where fluid is entering the domain, a pressure shear profile corresponding to the velocity shear profile is imposed. The remaining lower half of left border and upper half of right border keep the Non Reflecting Boundary Conditions imposed in the medium at rest; symmetry is also kept on upper and lower boundaries.

Although this is not visible on the vorticity contours of Figure 10, the evolution of the vortices is modified by the presence of the shear layer. Indeed, when a vortex is located in the upper half of the shear layer, its rotation is accelerated with the positive convection velocity toward the right; the inverse happens in the lower half shear layer. This is because the shear layer is added to the natural clockwise rotation of the vortices, inducing an increase of the rotation speed ω. Besides, during the rotation phase, the vortices rotation is not constant any more and is subject to variations, depending on the position of the vortices in the shear layer.

Due to the rotation speed increase, the vortices undergo merging sooner than in a medium at rest; here, the merging happens during the 8th rotation period and the rotation period is $3090\, \Delta t$. The pressure signal of Figure 11 is similar to the signal obtained in the previous case, while the disturbances of the mean pressure seem lower.

The dilatation is used once again to represent the acoustic radiation; in presence of a mean uniform

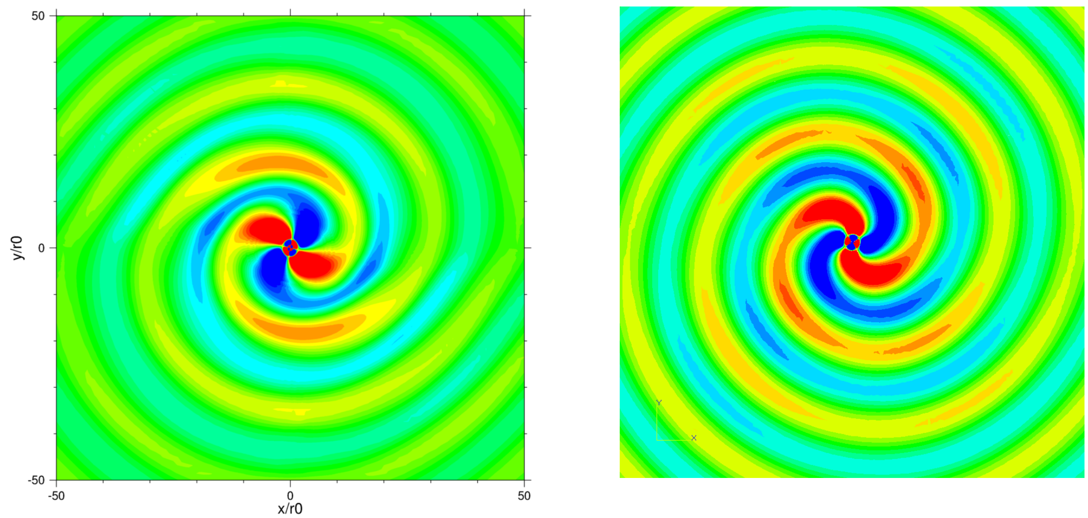

(a) (b)

Figure 12. Two corotating vortices placed in a shear layer. (a): Dilatation field obtained after 20000 time steps. Color levels from -50 to 50 s^{-1}. (b): Acoustic pressure field (real part) at the main radiation frequency f_a; color levels from -50 to 50 Pa. The domain extends spatially from $-50\,r_0$ to $50\,r_0$ in both directions.

unidirectional flow ΔU, the dilatation is related to the pressure time derivative by the following expression:

$$\Theta = -\frac{1}{\rho_0 c_0^2}\left(\frac{\partial p}{\partial t} \pm \Delta U \frac{\partial p}{\partial x}\right)$$

In Figure 12(a), the double spiral structure is again present, indicating a rotating quadrupole. The effects of the shear layer on the acoustic radiation are clearly visible. The wave fronts are deformed by the mean flow, having an oval shape instead of circular as in the medium at rest case. Moreover, the directivity is affected by the mean flow, with a favored radiation direction perpendicular to the mean flow, and lower levels in the main direction.

Acoustic results

As previously, the sound pressure level radiated at point $(50\,r_0, 50\,r_0)$ is reported in Figure 13 for the different computations: DNS, variational formulation with use of total and fluctuating source terms, and analytical formulation with use of total and fluctuating source terms. All spectra are found to collapse, excluding the DNS spectrum which presents a peak at the main radiation frequency 3 dB lower than the remaining spectra. This can be explained by the fact that in both variational and analytical formulations, the source term is defined on the central portion of the CFD domain extending from $-2.7\,r_0$ to $2.7\,r_0$ in both directions. Therefore, all refraction effects computed by DNS in the whole domain are missed in hybrid formulations, leading to a slightly different result.

However, in terms of radiation structure, the variational formulation is consistent; the acoustic pressure field shown in Figure 12(b) presents a destorted double spiral structure of oval shape, less pronounced than on the dilatation field of Figure 12(a) but still present. The privileged radiation directions are also similar to those of the direct computation.

III.A.3. Conclusion

The study of corotating vortices firstly placed in a medium at rest, and then in a shear layer, has shown the correct expression of the source term in the variational formulation of Lighthill's Acoustic Analogy: the source term S_i^t build on the total velocities has to be used. Secondly, the study with the shear layer sheds some light on the convection effects in Lighthill's Acoustic Analogy: the terms linked to pure convection in

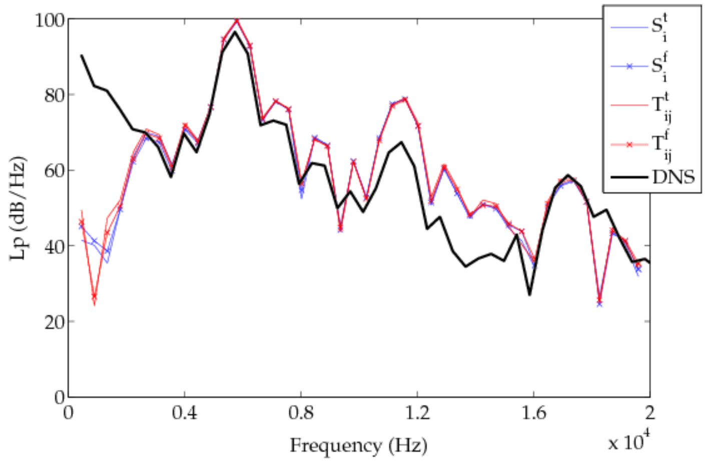

Figure 13. Two corotating vortices placed in a shear layer. Sound pressure level radiated at point $(50\,r_0, 50\,r_0)$ obtained with three different methods. Black: direct calculation; blue: variational formulation; red: analytical resolution of Lighthill's Acoustic Analogy. Without symbols: levels obtained using the total source terms S_i^t and T_{ij}^t. With symbols: levels obtained using the fluctuating source terms S_i^f and T_{ij}^f. Levels in dB.

Lighthill's tensor do not contribute to the radiated sound, on the contrary to the terms linked to a local mean velocity which can contribute significantly to the radiated sound. Moreover, in the variational formulation of Lighthill's Acoustic Analogy, acoustic waves refraction by a mean flow field can only be taken into account if the source terms are computed on the whole region where mean flow exists. Otherwise, as in the case of the two vortices placed in a shear layer, mean flow effects outside the source region are out of reach of the present method. The present investigation supports the discussion of Bogey *et al.*[13]

III.B. Spatial truncation of noise sources

The spatial extent of the source term has to be treated with great care; indeed, following several authors, refer to Casper *et al*[14] for instance, this study shows with the test case of a vortex convection through a virtual boundary that spatial truncation of noise sources creates spurious numerical noise of dipolar nature. While common sense would then lead to define a source region extended in the whole CFD region, the simulation time objective of the hybrid method rather leads to a selection of reduced noise source regions. In order to conciliate both aspects of the problem, a spatial filtering technique, derived from the work of Pérot,[15] is tested and shown to eliminate the effects of spatial truncation of noise sources.

The following study is focused on the convection of a vortex through a virtual boundary and its radiated noise. As the objective is to determine the best method to reduce spurious noise created at the boundary, and not to study the vortex evolution in the CFD code, the vortex is perfectly convected, without disturbances, within an analytical solution; the acoustic propagation is performed with the variational formulation of Lighthill's Acoustic Analogy as previously. Dissipation effects usually present in a CFD calculation are not taken into account. This is thus a very constraining test case, as in a real computation, a vortex is progressively dissipated with the convection and its energy decreases as moving toward the boundary.

III.B.1. Convection of a vortex through a virtual boundary: presentation

A two-dimensional vortex is initialized at the origin of the domain, whose extent is $-50\Delta < x < 750\Delta$ in the first direction and $-50\Delta < y < 50\Delta$ in the second direction. The mesh size Δ is constant in both directions: $\Delta = 5 \times 10^{-4}$ m. The vortex is initialized with the following velocity components:

$$\left\{ \begin{array}{rcl} u(x,y) & = & U_0 + a_0\, y\, \exp\left[-\dfrac{\ln 2}{(n\Delta)^2}(x^2+y^2)\right] \\[2ex] v(x,y) & = & -\,a_0\, x\, \exp\left[-\dfrac{\ln 2}{(n\Delta)^2}(x^2+y^2)\right] \end{array} \right.$$

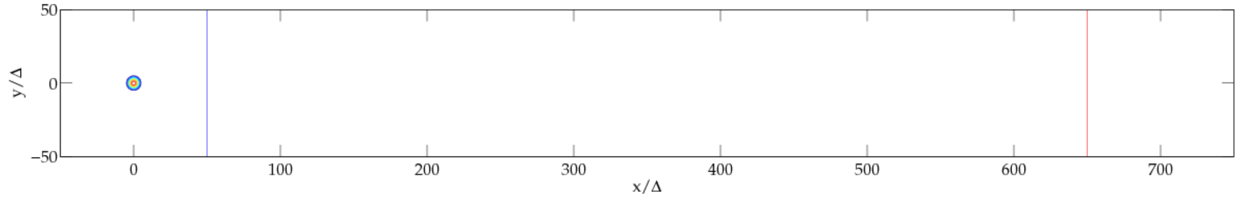

Figure 14. Initialization of the vortex. The vertical blue line indicates the location of $x_{\min}$, the vertical red line indicates the location of $x_{\max}$.

where U_0 is the convection velocity, and the constant $a_0 = 320\ \mathrm{m}^2/\mathrm{s}$ is chosen to verify that $u_{\max} = 2\,\mathrm{m/s}$ at a distance of $n\,\Delta$ from the vortex center. With this definition, the vortex diameter is $D = 2n\Delta$, and $n = 10$ and 5 successively in this study. The vortex is convected at velocity U_0 from $x = 0$ to $x = 0.35$, with the time step $\Delta t = \Delta/U_0$.

Regarding the acoustic propagation, the acoustic domain is a disk of radius 800Δ centered on the vortex origin at $t = 0$ and containing the mathematical region described previously. The mathematical mesh is kept for the acoustic mesh; in the remaining of the domain, the mesh is coarsened up to $\Delta_{\max} = 10\Delta$. Results are given in terms of acoustic power radiated by the whole domain, integrated on the circular boundary. For representation, the Strouhal number $St = fD/U_0$ is chosen where f is the frequency.

Spatial filtering is defined as a weight applied to the source terms before Fourier transformation. This weight is applied on distance $d = x_{\max} - x_{\min}$ (see Figure 14). $x_{\min}$ is fixed at 50Δ in the whole study, while $x_{\max}$ can vary, producing various filter lengths d. First of all, the filter length d is fixed at 600Δ and the filter shape is varied. Secondly, the best filter shape is chosen and the filter length d is adjusted.

III.B.2. Study on the filter shape

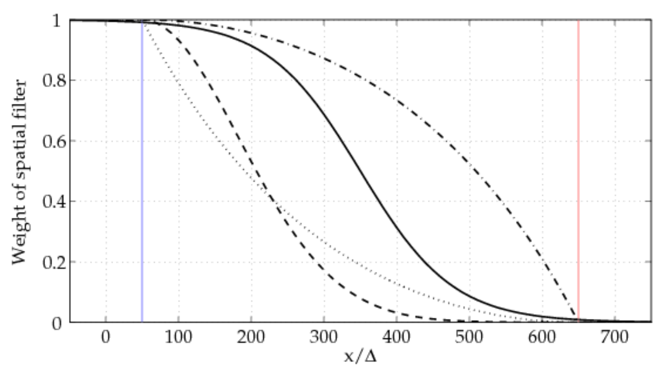

Figure 15. Spatial filters applied to the vortex convection case. The vertical blue line indicates the location of $x_{\min}$, the vertical red line indicates the location of $x_{\max}$. $\cdots\cdots$: $\mathcal{W}_1$; $-\cdot-\cdot-$: $\mathcal{W}_2$; $---$: $\mathcal{W}_3$; ——: $\mathcal{W}_4$.

The vortex diameter is fixed at $D = 20\Delta$, and the convection velocity is $U_0 = 2\,\mathrm{m/s}$. The filter length is thus $d = 600\Delta = 30D$: the filter is applied on a distance corresponding to 30 vortex diameters. The acoustic radiation produced by a sharp truncation of the source terms at $x = x_{\min}$, as well as four different filter shapes are compared; the reference case is obtained by analyzing the acoustic radiation of the vortex

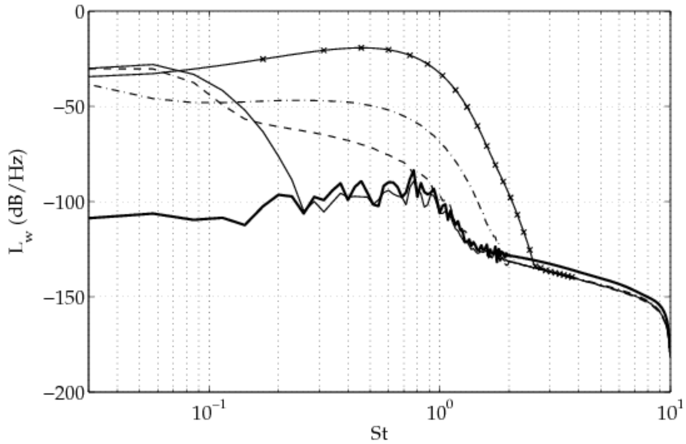

Figure 16. Acoustic power radiated by the vortex convection. Study on the filter shape. Bold solid line: reference case (no truncation, no filtering); —×—: sharp truncation at x_{min}; $- \cdot - \cdot -$: $\mathcal{W}_2$; $- - -$: $\mathcal{W}_3$; ——: $\mathcal{W}_4$.

convected without modification along the whole domain. The different filter weights are defined as follows:

$$
\begin{cases}
\mathcal{W}_1(x) &= -1 + \exp\left[\dfrac{(x_{\mathrm{max}} - x)^2}{2\sigma^2}\right] \\[2ex]
\mathcal{W}_2(x) &= 2 - \exp\left[\dfrac{(x - x_{\mathrm{min}})^2}{2\sigma^2}\right] \\[2ex]
\mathcal{W}_3(x) &= \exp\left\{-\dfrac{1}{2}\left[\dfrac{\alpha}{2}\dfrac{x - x_{\mathrm{min}}}{x_{\mathrm{max}} - x_{\mathrm{min}}}\right]^2\right\} \\[2ex]
\mathcal{W}_4(x) &= \dfrac{1}{2}\left\{1 + \tanh\left[-\dfrac{3\pi}{2d}\left(x - \dfrac{x_{\mathrm{min}} + x_{\mathrm{max}}}{2}\right)\right]\right\}
\end{cases}
$$

with $\sigma = d/\sqrt{2\ln 2}$ and $\alpha = 9$, and are displayed in Figure 15. Acoustic results are presented in Figure 16. The sharp truncation of noise sources at x_{min} produces a strong acoustic radiation in the low frequency range $St < 2.6$, with levels superior by more than 75 dB to the reference case, namely without truncation. Such a spurious acoustic radiation is often encountered when working with hybrid methods, when the acoustic terms are crossing the boundary of the region where they are considered. Casper *et al*[14] have shown that the spurious radiation is of dipolar nature. Filters $\mathcal{W}_1$ and $\mathcal{W}_2$ are symmetric and thus produce the same acoustic radiation; therefore, only the results associated to filter $\mathcal{W}_2$ are presented in Figure 16. The main observation is that all filters produce a spurious acoustic radiation. However, filters have a different impact on the acoustic power level. Indeed, filters $\mathcal{W}_2$ and $\mathcal{W}_3$, which are sharper than filter $\mathcal{W}_4$, radiate in a greater range of Strouhal numbers, respectively for $St < 1.8$ and $St < 1.1$, while the hyperbolic-tangent shaped filter $\mathcal{W}_4$ radiates only for $St < 0.26$. This last filter is thus retained for the remaining of the study.

III.B.3. Study on the filter length

In order to minimize the length of the sponge zone that will be used for spatial filtering of acoustic source terms, a study on the filter length is performed. Convection velocity is fixed at 5 m/s and the vortex diameter is now $D = 10\Delta$. Spatial filtering defined with the weight $\mathcal{W}_4$ is applied, and the filter length d is varied from $10\,D$ to $60\,D$. Acoustic results are presented in Figure 17. The filter length directly influences the critical frequency: the critical Strouhal number decreases from 0.6 to 0.18 when the filter length varies from $60\,D$ to $40\,D$. Then, a further decrease of the filter length d does not seem to improve significantly spectra.

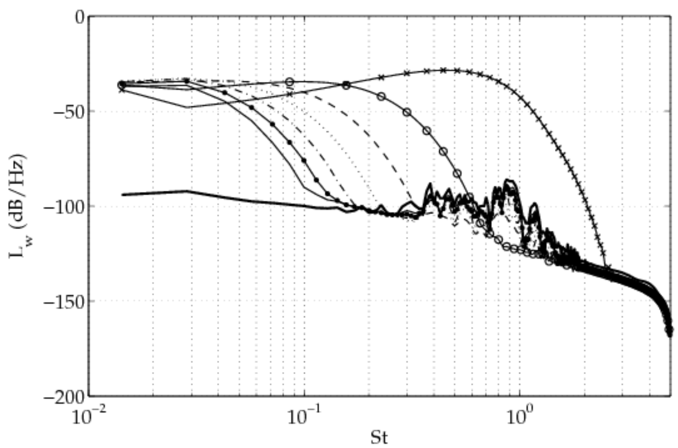

Figure 17. Acoustic power radiated by the vortex convection. Study on the filter length. Bold solid line: reference case (no truncation, no filtering); —×—: sharp truncation at $x_{\min}$; —○—: $d = 10D$; − − −: $d = 20D$; · · · · · ·: $d = 30D$; − · − · −: $d = 40D$; —•—: $d = 50D$; ——: $d = 60D$.

III.B.4. Conclusion

This study allows to state that using a spatial filtering of shape $\mathcal{W}_4$ on acoustic source terms on a distance of a few tenth of the structures diameters D should minimize the effects of spatial truncation above the critical Strouhal number $St = fU_0/D$, where U_0 is the convection velocity of the structures crossing the virtual boundary.

III.C. Interpolation of noise sources

As suggested in §II.D, noise sources computed within the flow simulation on the CFD mesh have to be interpolated on the acoustic mesh to be propagated to the desired locations. Indeed, the constraints are much more severe for the design of the CFD mesh than for the acoustic mesh, and the characteristic mesh sizes of both meshes differ by at least one order of magnitude in the source regions. Therefore, in order to keep an accurate definition of the sources, it is necessary either to refine the acoustic mesh in these regions to match the CFD mesh size, or to interpolate noise sources on a coarser acoustic mesh. The first solution is only tractable on small meshes; in real cases, such as for the diaphragm presented here below, keeping the CFD mesh accuracy for the acoustic mesh in the source regions would lead to a considerably heavy finite element model of several millions degrees of freedom. Therefore, an interpolation is performed to lighten the acoustic mesh.

As shown in previous studies,[16] a study on interpolation schemes can be performed to determine the best scheme for a given application. As expected, high order schemes and schemes based on Lagrange polynomials give the best results with a reduced interpolation error. However, they are only useful in a fully Cartesian framework. When working on non Cartesian meshes, as is the case in the diaphragm study (see §IV), even low order methods are difficult to handle. Therefore, and only for the diaphragm case study, the strategy is to record source data on a fully Cartesian mesh finer than the CFD mesh to retain accuracy, allowing thus the use of high order interpolation schemes.

IV. Case of a ducted diaphragm at low Mach number

IV.A. Presentation

The diaphragm geometry is presented in Figure 18; it is composed of a rectangular duct of section $D \times w = 80 \times 100\,\text{mm}$ obstructed by a diaphragm whose opening is rectangular of section $h \times w = 35 \times 100\,\text{mm}$. The diaphragm extends over $e = 5\,\text{mm}$, and the inlet and outlet ducts lengths are respectively $l = 95\,\text{mm}$ and $L = 500\,\text{mm}$. The aspect ratio defined as $A = w/h$ is equal to 2.85, and the expansion ratio defined as $R = D/h$ is 2.28. In this paper, flow and acoustics are studied for a very low Mach number flow, with the mean velocity $U_0 = 6\,\text{m/s}$ at the inlet, corresponding to $M = U_0/c_0 = 0.017$. The Reynolds number

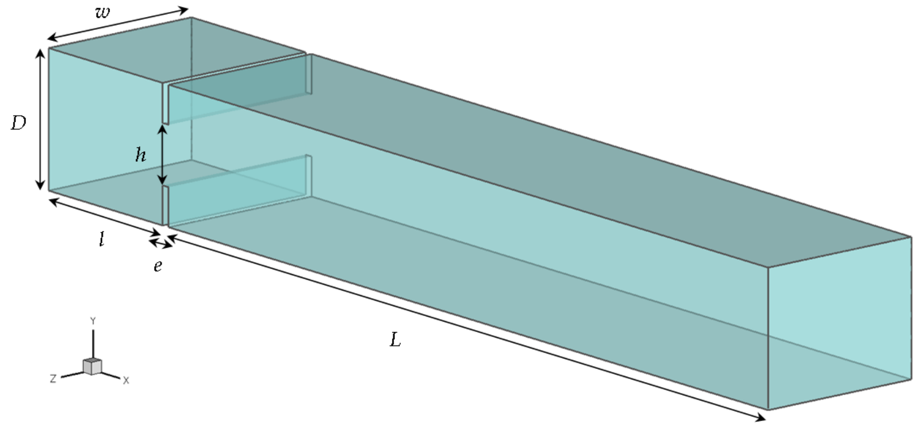

Figure 18. Diaphragm geometry. The aspect ratio is given by $A = w/h$, where w is the duct width and h the diaphragm opening; the expansion ratio is $R = D/h$, where D is the duct height. The x-axis indicated the streamwise flow direction; y- and z-axis respectively indicate the transverse and spanwise directions.

based on the inlet velocity U_0 and duct height D is $Re_D = 3.3 \times 10^4$, the Reynolds number computed at the diaphragm, based on the maximum bulk velocity $U_b = 20\,\mathrm{m/s}$ and obstruction height h, is $Re_h = 4.8 \times 10^4$. The flow is fully turbulent.

This case has been studied previously, in particular by Van Herpe *et al*[17] who performed experiments in order to get the acoustic power radiated by the diaphragm, and by Gloerfelt and Lafon[6] who performed a Direct Noise Computation, both providing reference results for the present simulation.

The aerodynamic features of the flow downstream a rectangular diaphragm is very similar to that downstream a plane sudden expansion. This last geometry has been extensively studied experimentally, and many authors provide detailed descriptions of the flow characteristics for different aspect and expansion ratios. These studies mainly aim at providing a physical explanation to the symmetry breaking, pitchfork bifurcation, occurring just behind the double step in a specific range of Reynolds numbers and aspect and expansion ratios. This asymmetry causes the flow to attach to one or the other wall parallel to the expansion; this phenomenon is sometimes called the Coanda effect in the literature. The experiments of Durst *et al*[18] demonstrate that the low Reynolds number flow downstream of a sudden expansion in a symmetric channel of large aspect ratio may be asymmetric and substantially three-dimensional. Cherdron *et al*[19] moreover provide a map of symmetric and asymmetric flow regions, depending on Reynolds number, aspect and expansion ratios; it is found that a decrease of the aspect and expansion ratios has a stabilizing effect, which extends the range of Reynolds numbers over which symmetric flow can exist. At higher Reynolds numbers, the small disturbances generated at the lip of the sudden expansion are amplified in the shear layers, shedding patterns which alternate from one side to the other with consequent asymmetry of the mean flow. Another general conclusion of Cherdron *et al*[19] is the ratio between both recirculation lengths: the smaller recirculation region length corresponds to a single wavelength of the disturbance, while the longer recirculation length is close to odd multiples of the disturbance wavelength, three in Cherdron *et al*[19] experiments.

Last reviews of Escudier *et al*[20] and Casarsa and Giannattasio[21] provide detailed experimental results for the case of turbulent flow through a plane sudden expansion (PSE) at high Reynolds numbers. In Escudier *et al*,[20] aspect and expansion ratios are $A = 5.33$ and $R = 4$ and the Reynolds number is fixed at $Re_h = 5.55 \times 10^4$. In addition to the asymmetry already noticed previously, three-dimensional effects are noticed with differences along the span; this behavior is attributed to the presence of two contra-rotating vortices located downstream the expansion, near the channel side walls, seemingly resulting from the modest aspect ratio. After a detailed analysis of PIV results of the flow through a planar sudden expansion of aspect and expansion ratios $A = 10$ and $R = 3$ and at a Reynolds number of 10^4, Casarsa and Giannattasio[21] propose a three-dimensional model of the complex flow field. In this model, a spanwise mass transport of spiral motion is associated to each recirculation; the mass loop is closed thanks to the presence of corner vortices in the vicinity of lateral walls.

It is interesting to note that all numerical experiments performed on planar sudden expansions report a natural evolution of the flow toward asymmetry, even when using Reynolds Averaged Navier-Stokes sim-

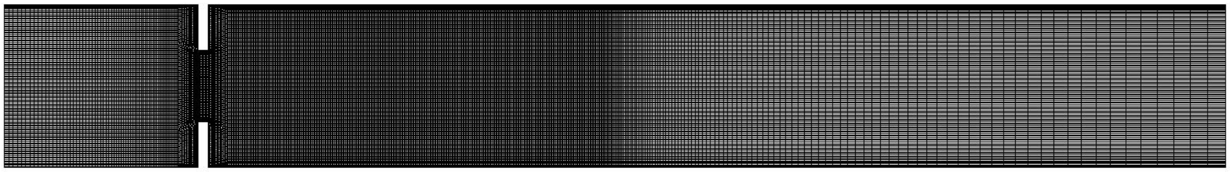

(a) Overall view of the mesh.

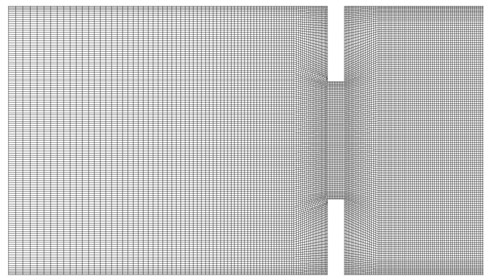

(b) Zoom on the inlet and diaphragm region.

Figure 19. Diaphragm mesh. Every line mesh is shown.

ulations, provided that the geometric and flow conditions are favorable to bifurcation and that a transient computation is led. Fearn *et al*[22] compute the two-dimensional flow field downstream of a plane sudden expansion ($R = 3$, $A = 8$) with a finite-element discretization of Navier-Stokes equations. An experimental bifurcation diagram is built; in order to reproduce the disconnection due to small imperfections in the experimental apparatus, the calculations are run with a 1% change in the geometry, grid shift with respect to the symmetry axis. Fearn *et al*[22] conclude that, considering the overall agreement in resulting diagrams, the bifurcation observed is a fundamental property of the Navier-Stokes equations.

Durst *et al*[23] study experimentally and numerically a plane sudden expansion of aspect and expansion ratios $A = 2$ and $R = 2$, at a high Reynolds number in the fully laminar region $Re = 610$. Three-dimensional effects are supposed weak, therefore a 2D finite element simulation is used. While a symmetric flow configuration was always assumed, flow bifurcation occurred without geometric inlet disturbances; Durst *et al*[23] attribute it to truncation errors which prevent a zero transverse velocity at the symmetry plane.

More recently, De Zilwa *et al*[24] assume that the flow through a plane sudden expansion of aspect ratio $A = 4$ and expansion ratio $R = 2.85$ is two-dimensional; they chose a transient $k - \epsilon$ modeling, and predicted the transition from symmetry to asymmetry at $Re = 90$. Detailed comparisons of velocity and r.m.s. profiles are given and compared to experimental results at low Reynolds numbers; the poor agreement is attributed to the turbulence modeling limitations, while missed three-dimensional effects could also be a source of errors.

Chiang *et al*[25] report an original behavior of the flow field where, in addition to the classical step height bifurcation, a spanwise bifurcation is observed when the channel aspect ratio exceeds a critical value; indeed, in this particular case, the step height symmetry breaking evolves with different symmetry breaking orientations on the left and right sides of the channel.

IV.B. Three-dimensional computation on whole geometry

IV.B.1. Mesh

The geometry is shown in Figure 18. The mesh used for the CFD computation, reported in Figure 19, is composed of 8 millions cells. A first two-dimensional structured mesh in the XY plane is built with 82×120 cells in the inlet duct, 10×66 cells in the diaphragm aperture and 428×130 cells in the outlet duct. In the x-direction, the mesh size is constant in the diaphragm aperture, $\Delta x = 0.5$ mm, and in the first half of the outlet duct, $\Delta x = 0.6$ mm. The mesh is then stretched to the inlet and outlet sections with the rates of 1.7 % and 2.75 % respectively, leading to the maximum cell size of 2.2 mm in the inlet duct and 8.8 mm in the outlet duct. In the y-direction, the mesh is constant in the diaphragm aperture, $\Delta y = 0.55$ mm, in the inlet

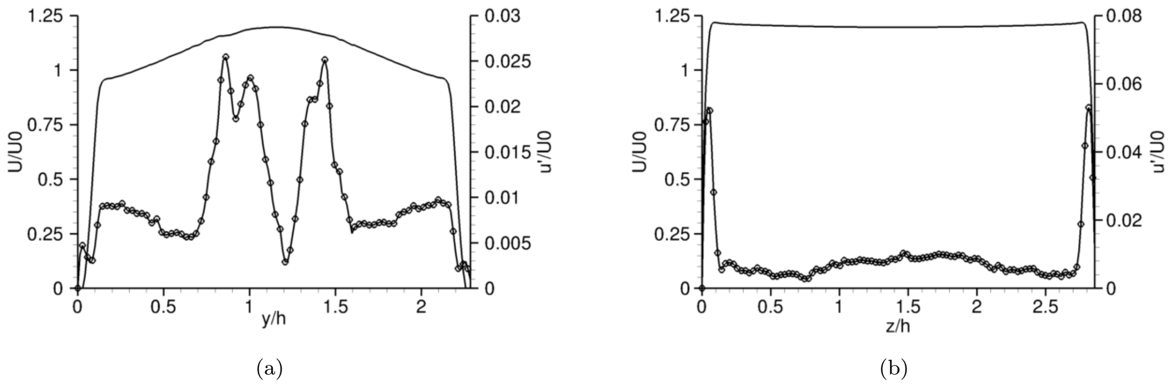

Figure 20. Diaphragm. Profiles of mean (solid) and rms (symbols) streamwise velocity components in the (a): XY midplane and (b): XZ midplane at $x/h = -1$.

duct, $\Delta y = 0.65\,\mathrm{mm}$, and in the outlet duct, $\Delta y = 0.63\,\mathrm{mm}$. Boundary layers consisting of local refinement are also defined near lower and upper walls with the first cell of size $\Delta y_{\mathrm{min}} = 0.35\,\mathrm{mm}$ and a stretching rate of 5 % on diaphragm walls and outlet duct walls, and 10 % on the inlet duct walls. The two-dimensional mesh is then extruded in the z-direction on 120 cells of size $\Delta z = 1\,\mathrm{mm}$ in the central region, with a local 5 % refinement near the lateral walls, with the minimum cell size $\Delta z_{\mathrm{min}} = 0.4\,\mathrm{mm}$.

IV.B.2. Numerical simulation parameters

An incompressible Large Eddy Simulation is performed on the previously described finite volume mesh. The Smagorinsky–Lilly subgrid-scale modeling is used with the constant value $C_S = 0.1$. Spatial discretization is central differencing of second order, and the time discretization is implicit of second order with the use of a Non Iterative Time Advancement (NITA) scheme. The time step is $\Delta t = 10^{-5}\,\mathrm{s}$, corresponding to a maximum Courant number of 0.78. A uniform constant velocity $U_0 = 6\,\mathrm{m/s}$ is imposed at the inlet boundary, and an outflow condition at the outlet boundary.

IV.B.3. Initial conditions

The initial conditions applied at the beginning of an unsteady CFD computation must, in the best case, represent a guessed solution of the mean flow field. In confined flow problems, starting from a medium at rest causes stability and convergence problems: in these problems, the pressure drop between the inlet and outlet plays a crucial role and must be steadily converged before starting the unsteady simulation. Therefore, for all computations presented here on the diaphragm geometry, a first Reynolds Averaged Navier-Stokes $k - \epsilon$ computation has been converged to second order and is used as an initial condition for LES.

A stable transient state is reached after approximately 0.2 s of physical time, that is to say 2000 time steps; the computation is then performed for another physical period of 0.1 s for statistics and source term recordings.

IV.B.4. Aerodynamic analysis

Upstream flow conditions

The check of inlet conditions allows to determine if the flow is fully developed and symmetric before the contraction; Figure 20(a) presents the streamwise velocity profiles upstream of the diaphragm in the XY midplane, normalized with the inlet velocity. The profiles are symmetric as expected, but characterize a non fully developed flow. The streamwise turbulent fluctuations in the XY midplane show to be of order 1 % of U_0, with peaks on both sides of the channel centerline reaching 2.5 %.

In the XZ midplane, the flow appears to be more developed as shown in Figure 20(b) by the profiles of mean and rms streamwise velocity profiles normalized by U_0. The mean velocity profile exhibits a plateau in the range $0.3 < z/h < 2.6$, which shows the uniformity of the inlet flow in the z-direction. Both profiles are again symmetric.

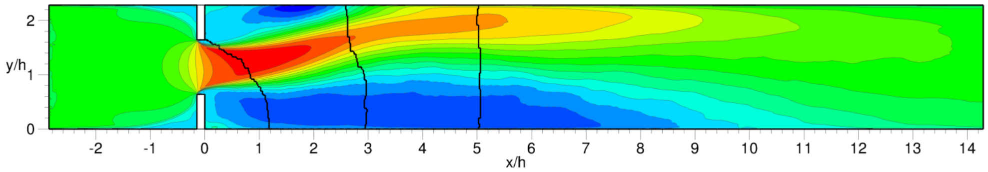

(a) U/U_b (color levels from -0.3 to 1)

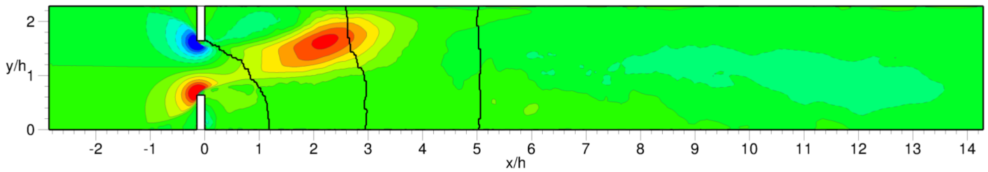

(b) V/U_b (color levels from -0.3 to 0.4)

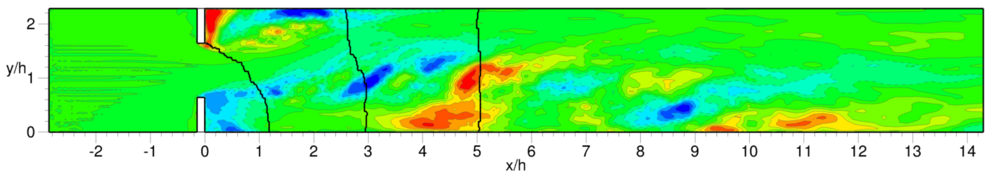

(c) W/U_b (color levels from -0.06 to 0.06)

Figure 21. Diaphragm. Mean velocity field in the XY midplane. Solid contours have positive values, dashed contours have negative values. Bold black lines indicate the position of partitions involved during the parallel computation, 4 of the 8 blocks are displayed here).

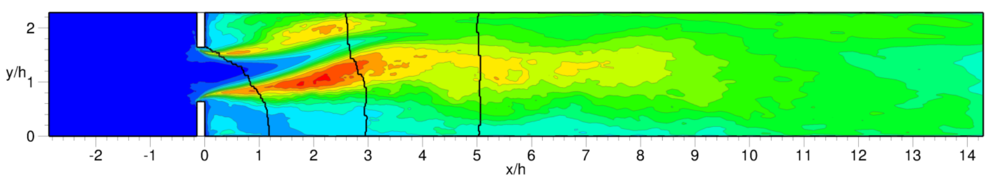

(a) u'/U_b (color levels from 0.02 to 0.26)

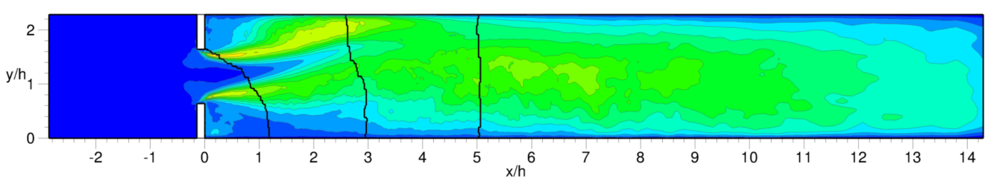

(b) v'/U_b (color levels from 0.02 to 0.26)

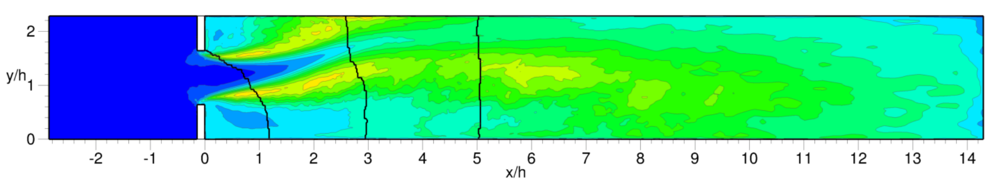

(c) w'/U_b (color levels from 0.02 to 0.26)

Figure 22. Diaphragm. r.m.s. turbulent velocities in the XY midplane.

IV.B.5. Mean flow in the XY midplane

As the averaged components of velocity illustrate it in Figure 21, the flow field can be divided in three regions. Upstream of the diaphragm, the flow is uniformly sucked by the contraction, producing very fine turbulent boundary layers near the walls. The jet-like flow emanating from the diaphragm then attaches to the top wall as observed in the case of plane sudden expansions, with the formation of two recirculation regions on both sides of the core flow. Each recirculation zone is composed of one primary large structure and one corner vortex near the diaphragm walls. Finally, in the second half of the outlet duct, the flow becomes more quiet with progressive detachment from the top wall and tends to become symmetric again. Note that the probability for the flow to exhibit one or the other stable solution is the same; in a previous calculations, the flow was found to attach to the bottom wall. No secondary attachment to the opposite wall is observed, as noticed for instance by Durst *et al*[18,23] or Fearn *et al*[22] in the case of PSE in the laminar flow regime. However, such a secondary attachment may be absent or masked by the too short length of the outlet duct, since the experimental results show it to appear around $x/h = 20$.

As already discussed, the mechanism of symmetry breaking leading to asymmetry results from a fundamental instability in Navier-Stokes equations when exceeding a critical Reynolds number, depending on the expansion geometry; this instability has two stable asymmetric solutions, with attachment to one or the other wall, and one unstable symmetric solution. It is clear that in the fully turbulent regime of the diaphragm, the critical Reynolds number is exceeded, and the large enough expansion ratio $R = 2.28$ allows the pitchfork bifurcation to occur. A smoother expansion can lead to a symmetric flow field even at a high Reynolds number, as shown experimentally by Smyth,[26] who found a symmetric field downstream of a double backward facing step of expansion ratio $R = 1.5$ and Reynolds number $Re_h = 2 \times 10^4$.

The overall agreement for mean and r.m.s. velocity contours with Gloerfelt & Lafon[6] is satisfactory, in terms of levels as well as regarding the position and extent of recirculation zones and boundary layers. The contours of mean streamwise velocity in Figure 21(a) shows that the maximum values of U/U_b follow the general direction of the flow toward the top wall. The largest back flow is located in the core of the large recirculation zone, near the walls, and reaches a value of $20\,\%\,U_b$ as noticed in previous studies.[20,21,23,24] Local minima and maxima of transverse mean velocity V are found at the upstream diaphragm lips, where the flow is accelerated through the contraction; in the outlet duct, a maxima is located in the lower shear layer just before the jet flow attach the top wall.

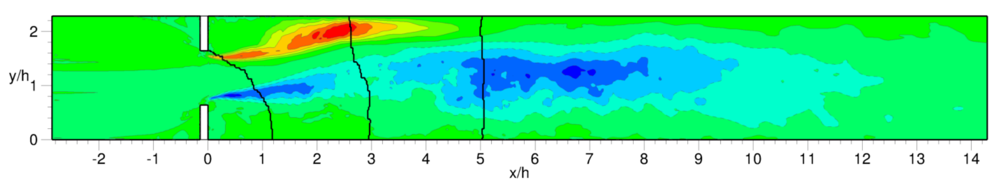

Figure 23. Diaphragm. Reynolds shear stress $\overline{u'v'}/U_b^2$ (color levels from -0.02 to 0.025) in the XY midplane.

Moreover, the r.m.s. turbulent velocities normalized by the bulk velocity U_b displayed in Figure 22 show a significant anisotropy with streamwise intensity levels in general higher than the transverse and spanwise ones. Local maxima are found in the shear layers before the attachment. The maximum value of the r.m.s. axial turbulence intensity is $u'/U_b|_{\max} \simeq 0.26$, consistent with that reported by Casarsa & Giannattasio[21] and Escudier *et al*;[20] resulting axial turbulence in the second half of the duct has a $15\,\%$ mean intensity, also consistent with previous studies. The transverse turbulence intensity reaches a maximum of $18\,\%U_b$ in the upper shear layer, consistent with Escudier *et al*[20] and sligthly higher than that of Casarsa & Giannattasio;[21] far downstream, the mean transverse turbulence intensity is still $10\,\%$ of U_b. The Reynolds shear stress $\overline{u'v'}$ presented in Figure 23 is consistent with the contours of U since its sign inversion occurs where the mean streamwise velocity is maximum. Maximum values about $2.5\,\%U_b^2$ are reached in the upper shear layer at the same downstream location as the peak of axial turbulence intensity; minima of $2\,\%U_b^2$ occur in the lower shear layer just downstream of the diaphragm.

The lengths of the primary recirculations L_1 and L_3 and of the secondary structures L_2 and L_4, as labeled in Figure 24, are defined as the positions where the mean streamwise velocity component changes sign. They are reported in Table 1 in the XY midplane. While the absolute values can hardly be compared to the values published previously, due to the wide range of PSE geometries and Reynolds numbers investigated, some tendencies can still be drawn. As reported by Casarsa & Giannattasio,[21] the reattachment lengths

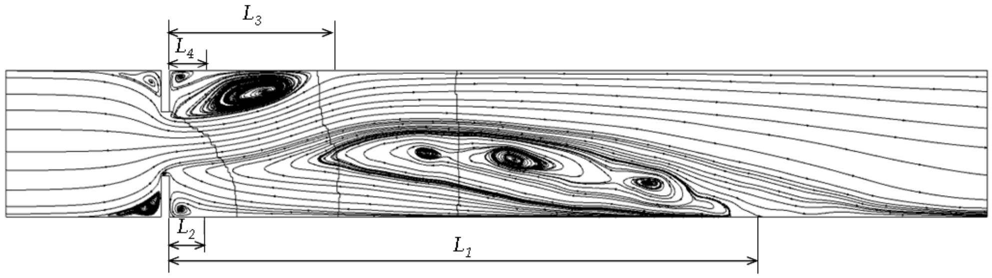

Figure 24. Diaphragm. Label of the different recirculations.

L_1/h	L_2/h	L_3/h	L_4/h
9.83	0.57	2.6	0.46

Table 1. Diaphragm. Normalized lengths of the primary and secondary recirculation zones in the XY midplane.

are mainly a function of the expansion ratio; for the case $R = 3$, the ranges provided by Abbott & Kline[27] are $L_1/h = 11 - 15$ and $L_3/h = 3.5 - 4$; the values reported here are substantially below these ranges, but considering the lower expansion ratio of this work, namely $R = 2.25$, the values found are consistent. Regarding the secondary recirculation lengths, the only reported values are from Casarsa & Giannattasio[21] and Spazzini *et al*,[28] with L_2 and L_4 of the order of one; it is twice the values found here, but no conclusion can be drawn taken the disparity in the considered geometries. Note also the presence of two corner vortices, just upstream of the diaphragm; their extent is also of order h.

Mean flow evolution along the span

As shown in Figure 25, where the mean path lines computed with the U and V components of the mean velocity field are drawn for three XY planes, the flow is not uniform along the span. Figure 26 also reports the evolution of the recirculation lengths along the span z/h. While the shorter recirculation L_3 remains almost constant, the longer recirculation L_1 undergoes great variations, with in particular a nearly uniform increase of $2h$ in the right channel half from the center to the wall. Regarding the secondary corner structures, their extent is almost uniform in the central portion of the channel, and opposite behaviors are found near the lateral walls: the lower recirculation zone extent is doubled near the left wall, while the upper one is nearly doubled in the vicinity of the right wall.

The three-dimensionality of the flow field can also be investigated by visualization of the flow paths in the XZ planes, as presented in Figure 27 for four y/h locations: in the lower recirculation region close to the wall ($y/h = 0.28$) and a bit upper ($y/h = 0.57$), in the midplane ($y/h = 1.1$), and in the upper recirculation, where the flow impinges the top wall ($y/h = 1.7$). In the lower recirculation, just above the channel floor, see Figure 27(a), two counter rotating vortices are found, resulting from the impingement of the big recirculation on the lower vertical diaphragm wall; the presence of these vortices was already proposed by Abbott & Kline[27] and confirmed by Casarsa & Giannattasio.[21] These vortices are still present at $y/h = 0.57$, see Figure 27(b), but the flow exhibits a much more complex behavior with several vortex structures counter rotating at the right and left of the channel centerline. In the midplane, see Figure 27(c), path lines are almost parallel since the jet-like flow is dominant in this plane. Upper at $y/h = 1.7$, see Figure 27(d), the location of flow separation is recognized, with the flow directed toward the diaphragm for $x/h < 0.6$ and toward the channel exit for $x/h > 0.6$.

In the light of figures 28 and 29, which present the mean axial and spanwise velocity contours at respectively $y/h = 0.57$ and $y/h = 1.7$, it is noticeable that, in the upper plane at $y/h = 1.7$, the axial mean velocity U is not constant along the span and have its minimum values of $-0.3\,U_b$ around the channel centerline. The spanwise mean flow W presents significant values only close to the diaphragm walls for $x/h < 0.2$, where the ground counter rotating vortices are present. In the upper plane at $y/h = 1.7$, the mean axial velocity contours are almost uniform along the span for $x/h < 2.2$, with the separation line between negative and positive velocities located at $x/h \sim 0.6$ as noticed in Figure 27(d). Around $x/h = 3$, two symmetrical maxima of U are found $z/h = 0.4$ and 2.4. The levels of spanwise velocity W in this plane are low, as indicated by the almost parallel path lines.

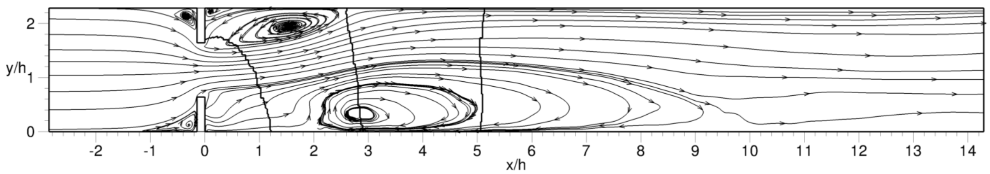

(a) $z/h = 0.28$

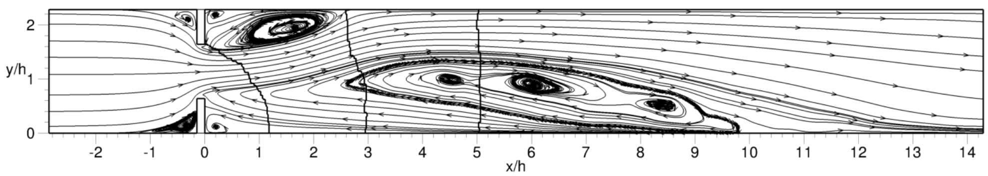

(b) $z/h = 1.4$ (midplane)

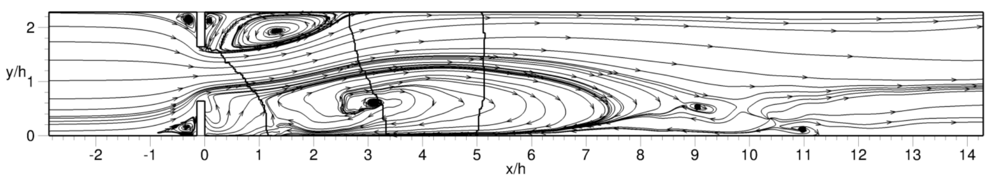

(c) $z/h = 2.6$

Figure 25. Diaphragm. Streamlines in XY planes computed with the U and V components of the three dimensional mean velocity field at different spanwise locations.

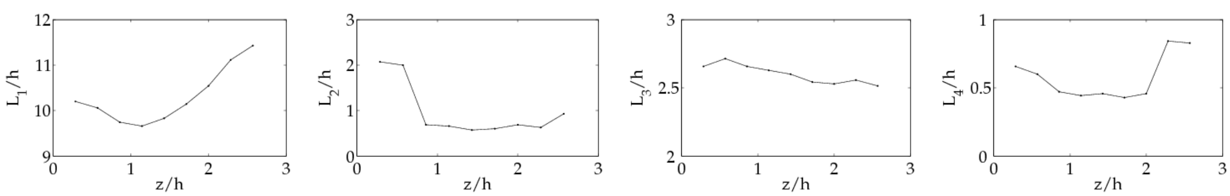

(a) (b) (c) (d)

Figure 26. Diaphragm. Recirculation lengths evolution, normalized by h, with respect to the position along the span.

Finally, the flow paths in section cuts as shown in Figure 30 allow to complete the understanding of this complex flow structure. In the first planes of figures 30(a)-(c), the flow paths are vertical for $0.8 < y/h < 1.5$, which corresponds to the core flow and shear layers. However, this behavior is perturbed near the walls for $z/h < 0.3$ and $z/h > 2.5$, where the interaction between the primary recirculations and corner vortices produce a complex flow. From $x/h = 2$, two counter rotating structures develop in the lower corners; these structures are created just downstream of the ground counter vortices noticed in Figure 27(a) and extend over the whole longer recirculation zone.

Instantaneous flow features

In Figures 31, 32 and 33 are presented the instantaneous contours of, respectively, streamwise, transverse and spanwise velocity, in the XY and XZ center planes and one YZ view. The jet unsteadiness is clearly visible, with the periodic shedding of structures from the lips of the diaphragm. The three-dimensional development and the range of turbulent structures is representative of the computational level of refinement; in particular, small scale structures, characteristic of high Reynolds number flows, are present. The levels and the general aspect of this instantaneous flow field conform to that shown in Gloerfelt and Lafon.[6]

An alternative way of representing turbulence structures is obtained by visualizing the positive $\mathcal{Q}$ criterion,

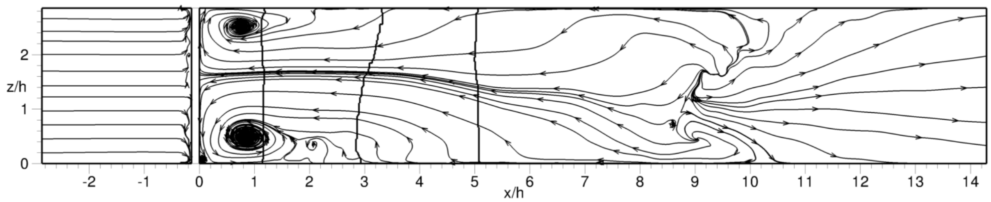

(a) $y/h = 0.28$

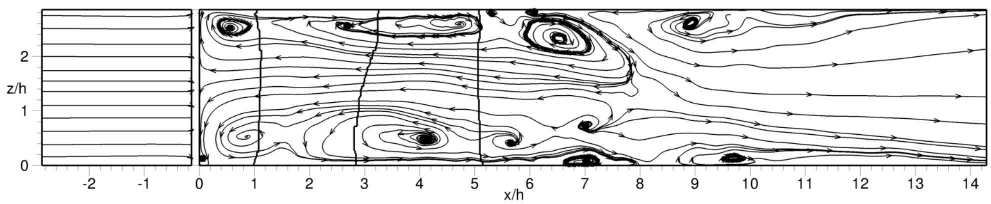

(b) $y/h = 0.57$

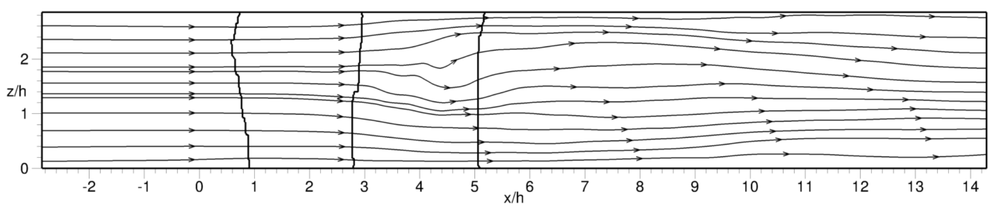

(c) $y/h = 1.1$ (midplane)

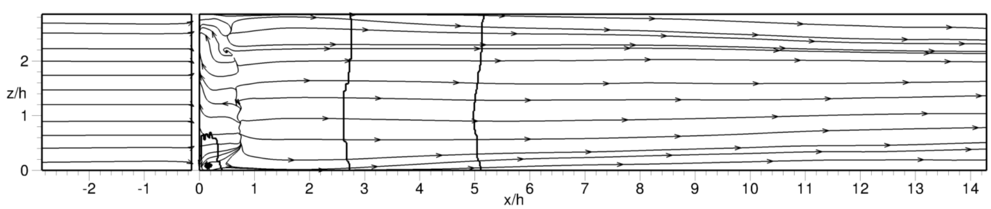

(d) $y/h = 1.7$

Figure 27. Diaphragm. Streamlines in XZ planes computed with the U and W components of the three dimensional mean velocity field at different height locations.

defined as the second invariant of velocity gradient tensor $\nabla\mathbf{u}$, Hunt *et al.*:[29]

$$\mathcal{Q} = \frac{1}{2}\left(\|\mathbf{\Omega}\| - \|\mathbf{S}\|\right)$$

where $\mathbf{\Omega}$ and $\mathbf{S}$ are the antisymmetric and symmetric parts of the velocity gradients $\nabla\mathbf{u}$. Figure 34 represents three views of the $\mathcal{Q}$ criterion normalized with $(U_b/h)^2$. The identified coherent structures are located in the shear layers. Close to the diaphragm, in the thin shear layers, the structures are well organized; the first series of structures generated by a Kelvin-Helmholtz instability are almost parallel to the z-axis with a nearly cylindrical shape. Further downstream, their orientation changes, and the structures are progressively split and turn in the main flow direction as the shear layers thicken. After the flow impinges on top wall, the structures rapidly disappear.

IV.B.6. Acoustic simulation

The acoustic mesh is built to retain maximum accuracy in the source term description in the region $-0.16 < x/h < 0.7$ where most sources are located; in this region, the mesh size is uniform: $\Delta x = \Delta y = \Delta z = 2\,\mathrm{mm}$ and the finite elements are wedge. In the remaining of the domain, tetrahedral cells are chosen with a maximum size of $10\,\mathrm{mm}$ to accurately propagate acoustic waves up to $f_{\max} = 5600\,\mathrm{Hz}$. As in the case of

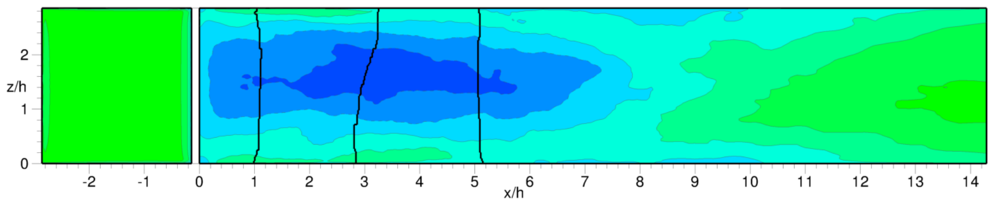

(a) U/U_b (color levels from -0.3 to 1)

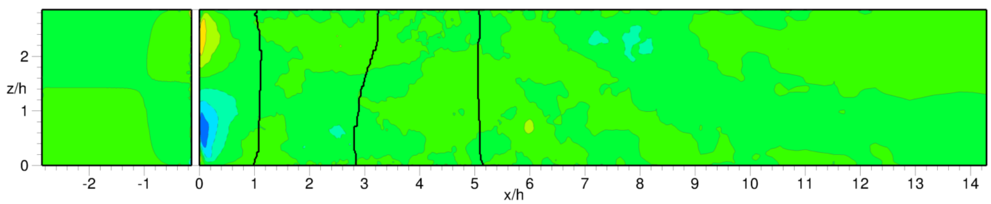

(b) W/U_b (color levels from -0.06 to 0.06)

Figure 28. Diaphragm. Mean velocity field in the XZ plane located at $y/h = 0.57$.

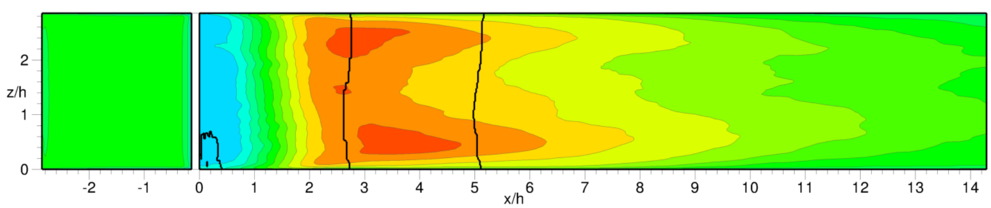

(a) U/U_b (color levels from -0.3 to 1)

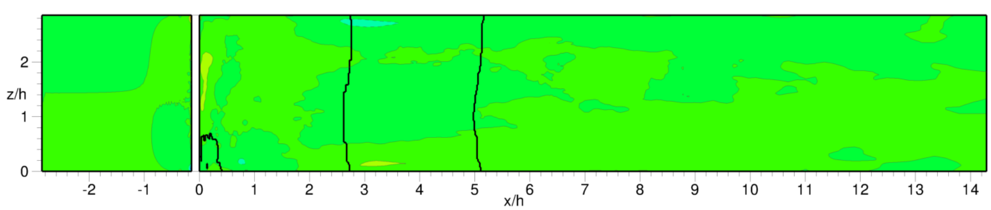

(b) W/U_b (color levels from -0.06 to 0.06)

Figure 29. Diaphragm. Mean velocity field in the XZ plane located at $y/h = 1.7$.

corotating vortices, a Fast Fourier Transform is performed on the transient signals after detrending and application of a Hanning filtering. The CFD time step $\Delta t = 10^{-5}$ s allows reaching the maximal frequency $f_{\max} = 5000$ Hz. The total recorded physical time T drives the frequency resolution f_r with $f_r = 1/T = 50$ Hz. As explained in §III.C, the strategy for interpolation in the diaphragm case is to define an intermediate Cartesian mesh finer than the CFD mesh where source terms are recorded. High order interpolation is then possible from this intermediate mesh to the acoustic mesh. Thus, a first 4th order Lagrange polynomial interpolation is performed in the z-direction, then a two-dimensional second order linear interpolation is applied in the XY planes. Indeed, performing the interpolation successively on different directions has been shown more efficient and less subject to errors than interpolating in all directions at the same time. The acoustic simulation is currently in progress.

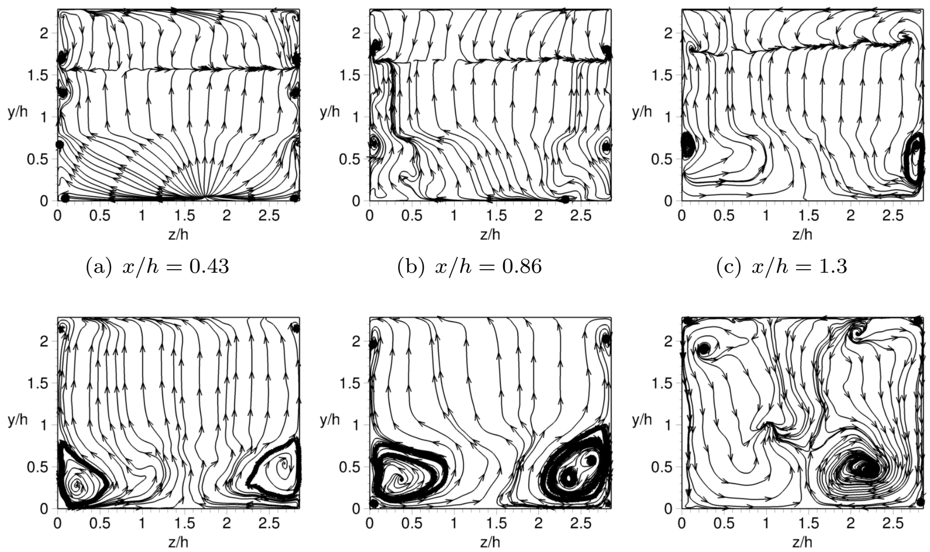

(a) $x/h = 0.43$ (b) $x/h = 0.86$ (c) $x/h = 1.3$

(d) $x/h = 2$ (e) $x/h = 2.8$ (f) $x/h = 6.3$

Figure 30. Diaphragm. Streamlines in YZ planes computed with the V and W components of the three dimensional mean velocity field at different longitudinal locations.

V. Conclusion

In this work, a hybrid method of aeroacoustic noise computation based on the variational formulation of Lighthill's Acoustic Analogy is presented and discussed; it involves the coupling of two commercial codes: a CFD code where incompressible Large Eddy Simulation is performed and a spectral finite element acoustic code. Complex geometries, low Mach number and internal flows, often encountered in industrial context, are adequate candidates for this method. The realization of several academic studies has allowed to establish and to validate the implementation, with numerical experiments to overcome the drawbacks intrinsically linked to the use of a hybrid method; in particular, the source term expression was justified. Realistic application of this simulation technique to the case of a ducted diaphragm at low Mach number requires a complete Large Eddy Simulation at full scale; comparisons with similar studies in the literature show that the turbulent flow field is well-resolved. The acoustic simulation is currently in progress.

Acknowledgments

The present work was supported by a fellowship of the Ministère de la Culture, de l'Enseignement Supérieur et de la Recherche of Luxembourg. The authors would also like to gratefully acknowledge Daniel Juvé and Christophe Bogey for fruitful discussions. Many thanks to Henri Clesse for initiating and supporting this research work from the beginning.

References

[1]Curle, N., "The influence of solid boundaries upon aerodynamic sound," *Proceedings of the Royal Society of London*, Vol. 231A, No. 1187, 1955, pp. 505–514.

[2]Lighthill, M., "On sound generated aerodynamically. Part I: General theory," *Proceedings of the Royal Society of London*, Vol. A211, 1952, pp. 564–587.

[3]Ffowcs Williams, J. E. and Hawkings, D. L., "Sound generated by turbulence and surfaces in arbitrary motion," *Philosophical Transactions of the Royal Society of London*, Vol. A264, 1969, pp. 312–342.

[4]Free Field Technologies, *Actran 2006 – Aeroacoustic solutions, User's manual*, 2006.

[5]Fluent Inc., *Fluent 6.3 User's Guide*, Sept. 2007.

[6]Gloerfelt, X. and Lafon, P., "Direct computation of the noise induced by a turbulent flow through a diaphragm in a duct at low Mach number," *Computers & Fluids*, Vol. 37, No. 4, 2008, pp. 388–401.

[7]Oberai, A. A., Ronaldkin, F., and Hughes, T. J. R., "Computational procedures for determining structural-acoustic response due to hydrodynamic sources," *Computer Methods in Applied Mechanics and Engineering*, Vol. 190, 2000, pp. 345–

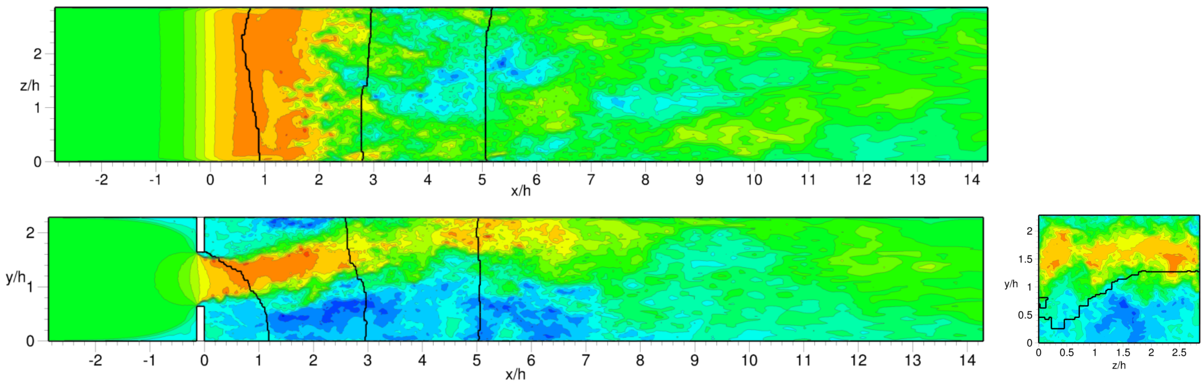

Figure 31. Diaphragm. Instantaneous longitudinal velocity u (color levels between -10 and $25\,\mathrm{m/s}$). Top, top view in the XZ midplane; bottom left, front view in the XY midplane; bottom right, cross section at $x/h = 2.8$.

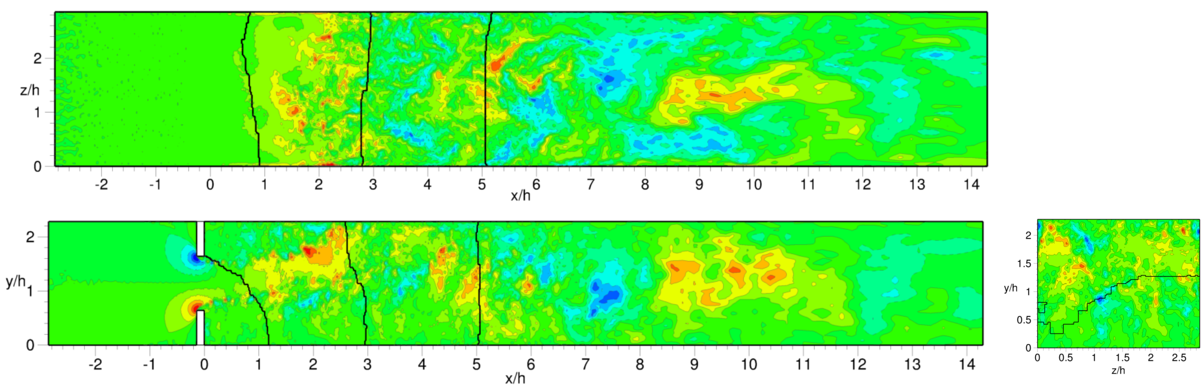

Figure 32. Diaphragm. Instantaneous crossflow velocity v (color levels between -10 and $10\,\mathrm{m/s}$). Top, top view in the XZ midplane; bottom left, front view in the XY midplane; bottom right, cross section at $x/h = 2.8$.

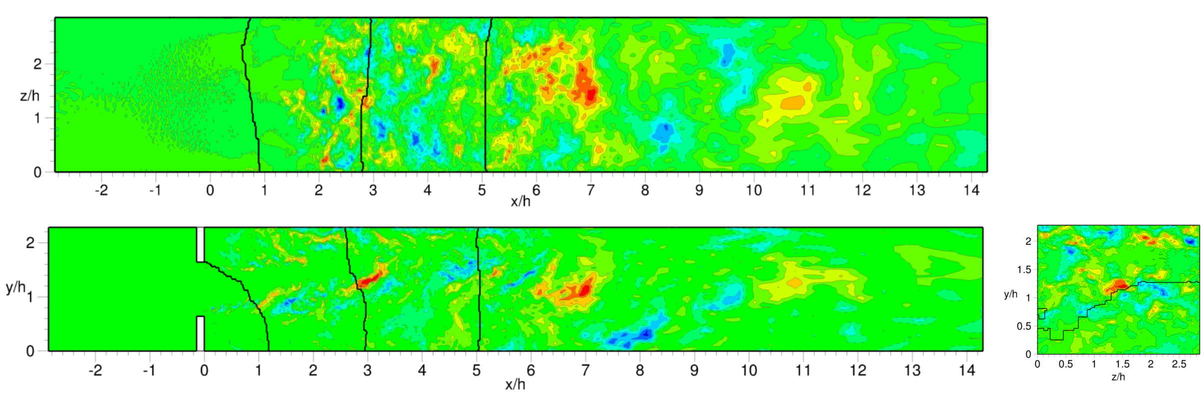

Figure 33. Diaphragm. Instantaneous spanwise velocity w (color levels between -10 and $10\,\mathrm{m/s}$). Top, top view in the XZ midplane; bottom left, front view in the XY midplane; bottom right, cross section at $x/h = 2.8$.

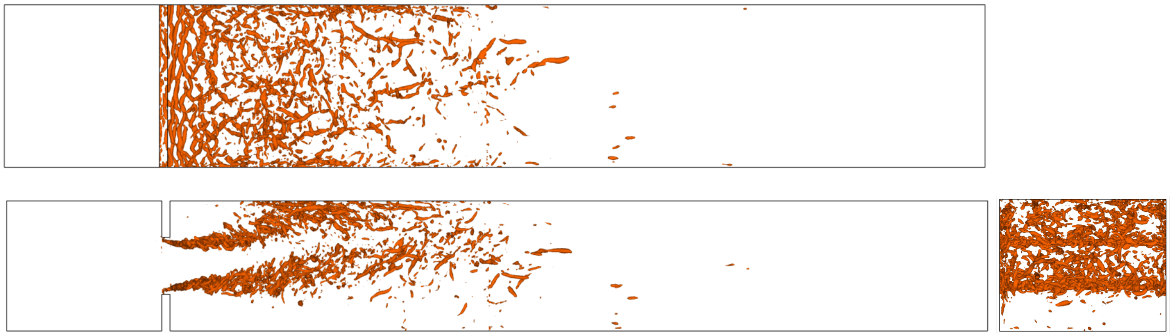

Figure 34. Diaphragm. Three dimensional isosurfaces of $\mathcal{Q}/(U_b/h)^2 = 10$. Top, top view; bottom left, front view; bottom right, side view.

361.

[8]Sandbodge, R., Caro, S., Ploumhans, P., Ambs, R., Schillemeit, B., Walshburn, K. B., and Shakib, F., "Validation of a CAA formulation based on Lighthill's analogy using AcuSolve and Actran/LA on an idealized automotive HVAC blower and on an axial fan," No. AIAA Paper 2006–2692, AIAA/CEAS Aeroacoustics Conference, 2006.

[9]Bogey, C., Bailly, C., and Juvé, D., "Numerical simulation of sound generated by vortex pairing in a mixing layer," *AIAA Journal*, Vol. 38, No. 12, 2000, pp. 2210–2218.

[10]Bogey, C., *Calcul direct du bruit aérodynamique et validation de modèles acoustiques hybrides*, Ph.D. thesis, Ecole Centrale de Lyon, France, 2000, (in French).

[11]Powell, A., "Theory of vortex sound," *Journal of the Acoustical Society of America*, Vol. 36, No. 1, 1964, pp. 177–195.

[12]Mitchell, B. E., Lele, S. A. K., and Moin, P., "Direct computation of the sound from a compressible co-rotating vortex pair," *Journal of Fluid Mechanics*, Vol. 285, 1995, pp. 181–202.

[13]Bogey, C., Bailly, C., and Juvé, D., "Computation of flow noise using source terms in linearized Euler equations," *AIAA Journal*, Vol. 40, No. 2, 2002, pp. 235–243.

[14]Casper, J. H., Lockard, D. P., Khorrami, M. R., and Streett, C. L., "Investigation of volumetric sources in airframe noise simulations," No. AIAA Paper 2004–2805, AIAA/CEAS Aeroacoustics Conference, 2004.

[15]Pérot, F., *Calcul du rayonnement acoustique d'écoulements turbulents basé sur des analogies acoustiques couplées aux simulations aérodynamiques instationnaires*, Ph.D. thesis, Ecole Centrale de Lyon, France, 2004, (in French).

[16]Marsden, O., *Calcul direct du rayonnement acoustique de profils par une approche curviligne d'ordre élevé*, Ph.D. thesis, Ecole Centrale de Lyon, France, 2005, (in French).

[17]van Herpe, F., Crighton, D. G., and Lafon, P., "Noise generation by turbulent flow in a duct obstructed by a diaphragm," No. AIAA Paper 95–035, AIAA/CEAS Aeroacoustics Conference, 1995.

[18]Durst, F., Melling, A., and Whitelaw, J. H., "Low Reynolds number flow over a plane symmetric sudden expansion," *Journal of Fluid Mechanics*, Vol. 64, No. 1, 1974, pp. 111–128.

[19]Cherdron, W., Durst, F., and Whitelaw, J. H., "Asymmetric flows and instabilities in symmetric ducts with sudden expansions," *Journal of Fluid Mechanics*, Vol. 84, No. 1, 1978, pp. 13–31.

[20]Escudier, M. P., Oliveira, P. J., and Poole, R. J., "Turbulent flow through a plane sudden expansion of modest aspect ratio," *Physics of Fluids*, Vol. 14, No. 10, 2002, pp. 3641–3654.

[21]Casarsa, L. and Giannattasio, P., "-dimensional features of the turbulent flow through a planar sudden expansion," *Physics of Fluids*, Vol. 20, 2008.

[22]Fearn, R. M., Mullin, T., and Cliffe, K. A., "Nonlinear flow phenomena in a symmetric sudden expansion," *Journal of Fluid Mechanics*, Vol. 211, 1990, pp. 595–608.

[23]Durst, F., Pereira, J. C. F., and Tropea, C., "The plane symmetric sudden-expansion flow at low Reynolds numbers," *Journal of Fluid Mechanics*, Vol. 248, 1993, pp. 567–581.

[24]De Zilwa, S. R. N., Khezzar, L., and Whitelaw, J. H., "Flows through plane sudden-expansions," *International Journal for Numerical Methods in Fluids*, Vol. 32, 2000, pp. 313–329.

[25]Chiang, T. P., Sheu, T. W. H., Hwang, R. R., and Sau, A., "Spanwise bifurcation in plane-symmetry sudden-expansion flows," *Physical Review E*, Vol. 65, 2001.

[26]Smyth, R., "Turbulent flow over a plane symmetric sudden expansion," *Journal of Fluids Engineering*, Vol. 101, 1979, pp. 348–353.

[27]Abbott, D. E. and Kline, S. J., "Experimental investigation of subsonic turbulent flow over single and double backward facing steps," *Journal of Basic Engineering*, Vol. 84, 1962.

[28]Spazzini, P. G., Iuso, G., Onorato, M., Zurlo, N., and Di Cicca, G. M., "Unsteady behavior of back-facing step flow," *Experiments in Fluids*, Vol. 30, 2001, pp. 551–561.

[29]Hunt, J. C. R., Wray, A. A., and Moin, P., "Eddies, Streams, and Convergence zones in turbulent flows," Proceedings of the Summer Program 1988, Center for Turbulence Research, 1988, pp. 193–208.